Glassy quantum nuclear pasta in neutron star crusts

William G. Newton ●,* Sarah Cantu, Shuxi Wang ●, and Amber Stinson ●
Department of Physics and Astronomy, Texas A&M University-Commerce, Commerce, Texas 75429-3011, USA

Mark Alexander Kaltenborn ●
Department of Physics, The George Washington University, Washington DC 20052, USA
and The Computational Physics and Methods Group, Los Alamos National Laboratory, Los Alamos, New Mexico 87545, USA

Jirina Rikovska Stone
Department of Physics and Astronomy, University of Tennessee, Knoxville, Tennessee 37996, USA;
Physics Division, Oak Ridge National Laboratory, Oak Ridge, Tennessee 37831, USA;
and Department of Physics, University of Oxford, Oxford, United Kingdom

We conduct a comprehensive survey of the shape parameter space of the nuclear pasta phases in neutron star crusts by conducting three-dimensional Hartree-Fock+BCS calculations. Spaghetti, waffles, lasagna, bicontinuous phases and cylindrical holes occupy local minima in the resulting constant-pressure Gibbs energy surfaces, implying multiple geometries coexist at a given depth. Notably, the bicontinuous phase, in which both the neutron gas and nuclear matter extend continuously in all dimensions appears over a large depth range. Our results support the idea that nuclear pasta is a glassy system. At a characteristic temperature, of order 10^8–10^9 K, different phases may become frozen into domains whose sizes we estimate to be 1–50 times the lattice spacing and over which the local density and electron fraction can vary. Above this temperature, very little long-range order exists and matter is an amorphous solid. Electron scattering off domain boundaries may contribute to the disorder resistivity of the pasta phases. Annealing of the domains may occur during cooling; repopulating of local minima during crustal heating might lead to temperature-dependent transport properties in the deep crust layers. We identify four regions distinguished by whether pasta is the true ground state, and whether the pasta structure allows delocalization of protons. The whole pasta region can occupy up to 70% of the crust by mass and 25% by thickness, and the layer in which protons are delocalized could occupy 45% of the crust mass and 15% of its thickness.

I. INTRODUCTION

As one moves deeper into the solid neutron star crust, passing through the outer crust stabilized by degenerate electrons and the inner crust stabilized by neutrons that have leaked out of the neutron-rich nuclei forming the crystal lattice, the nuclei occupy an increasing volume of the matter. Soft-matter systems on Earth give clues about what to expect as the separation between nuclei become comparable with their size [1]. When two fluid phases exist with one increasingly concentrated with respect to another, matter is self-organized into a number of different geometries. For example, aggregates of amphiphilic molecules called micelles arrange themselves into spherical, cylindrical, and planar phases with increasing concentration in water [2]. This phenomenon of self-orgnization can be understood to arise from frustration: the microscopic components of the system are subject to a competition between interactions operating over similar length scales. The total energy cannot be minimized with respect to all these microscopic interactions simultaneously. There is not single potential well for the system to fall into; instead a rich energy landscape of local minima separated by energy barriers of varying heights emerges. Small changes in the initial conditions of the system could lead to the microscopic constituents arranging themselves in different ways. Such materials are expected to have complex low-energy dynamics, giving rise to correspondingly complex behaviors of thermal conductivities, electrical resistivities and elastic properties.

Our system of interest comprises a Coulomb lattice of nuclei immersed in a fluid of neutrons. The microscopic interactions in play are the nuclear force and the Coulomb interaction. Throughout most of the inner crust, the short range nuclear interaction binds nuclei while the long rang Coulomb interaction drives the formation and stability of the lattice, determining the spacing between nuclei. As we move deeper toward the crust-core transition, however, the separation between nuclei becomes comparable with the length scale of the nuclear interaction ~ 10 fm and frustration is expected to ensue.

Consequences of this convergence of length scales was first studied by examining the compromise between surface

and bulk Coulomb energies of the nuclei in a liquid drop model and led to the conclusion that a sequence of exotic nuclear geometries became preferable at $\approx 0.5\rho_{cc}$ where ρ_{cc} is the crust core transition density [3–6]. Cylindrical, planar, cylindrical hole, and spherical hole configurations were found to be energetically favored with increasing density; the community has embraced a terminology based on the resemblance of the shapes to different forms of pasta [7], with the above sequence often referred to as spaghetti, lasagna, antispaghetti (or bucatini [8]) and antignocchi (with spherical nuclei cast as gnocchi). Pasta phases also persist at high temperature [9]. More recently, phases intermediate to this canonical sequence have been explored, with perforated planar configurations appearing between cylindrical and planar phases (nuclear waffles [10]), planar phases with helical connectors between sheets (parking garage structures [11]) and bicontinuous-P and gyroid phases mediating the transition between between planar and cylindrical holes [12–14] (we are awaiting the development of pasta forms that mimic many of these phases). Many of these find counterparts in the world in soft condensed matter [11,15]. The behavior of soft condensed matter systems suggests we should expect complex, potentially nonisotropic elastic and transport properties in nuclear pasta.

The state-of-the-art simulating nuclear pasta over the past two decades encompasses three dimensional quantum mean-field simulations using relativistic and nonrelativistic energy density functionals (EDFs) [14,16–28], and classical and quantum molecular dynamics simulations which access larger computational volumes but incorporate more schematic nuclear forces [10,11,29–46]. Microscopic quantum mean-field calculations demonstrated the complexity of the energy landscape of nuclear pasta which was shown to be enhanced by quantum shell effects [16]. This strongly suggests the possibility that pasta is highly disordered and amorphous with multiple different nuclear shapes coexisting at a given depth in the crust. Larger scale molecular dynamics simulations reveal other sources of disorder: for example, from topological defects in pasta [36], in which planar phases develop defects in the form of bridges between adjacent sheets.

As the crust cools, microscopic domains of different pasta phases may form at the same crust depth [38] which may persist on long timescales before annealing [47]. Individual domains could have highly anisotropic elastic and transport properties [48–50], for example, arising because of the difference between electron scattering parallel to spaghetti and lasagna structures and perpendicular to them. However, averaging over domains may render them more isotropic at the macroscopic level and reduce the resistive effect of pasta [48]. However, the existence of domains could give rise to another source of resistivity: electron scattering off domain boundaries. Thermal fluctuations may destroy the long-range order of pasta [47,51] and may set the length scale of domains; those length scales will determine if the rate of electron scattering rate off domain boundaries is important for the overall resistivity of the crust.

Pasta could account for 50% of the crust by mass [52,53], so there are observational consequences to the microscopic organization of pasta. The increased resistivity of disordered pasta could lead to potentially observable effects on the cooling curves of x-ray binaries [54] and the evolution of pulsar magnetic fields [55].

Given that there are many low lying minima separated by energy barriers, perhaps the best terrestrial analog is a glass: solids which, when heated, pass through an amorphous phase before melting. One possible scenario is as follows: as the neutron star cools below a characteristic temperature set by the energy barriers between local minima (either early in its life or after a period of accretion-induced crustal heating), amorphous nuclear pasta undergoes a transition in which it becomes frozen into coexisting domains of a certain length scale. Annealing may then take place on a timescale that is uncertain but could be long compared to, for example, the cooling timescale of the crust. The energy spectrum of the pasta phases, and the typical temperature and length scales in play in this scenario, are the subject of this paper.

We aim to map out the energy surfaces of nuclear pasta at a variety of densities by performing a large number of three-dimensional Skyrme-Hartree-Fock+BCS (3DHF+BCS) simulations at zero temperature and at proton fractions around β-equilibrium. Although our simulations are restricted to smaller computational volumes than molecular dynamics simulations, we can access zero temperature and lower proton fractions. Most calculations are performed at a given density; however, a given depth in the crust is defined by its pressure. To examine coexisting domains, energy surfaces at constant pressure must be calculated; the Gibbs free energy is the relevant quantity to compare different phases. We will interpolate between calculations over a range of densities to find the configurations at a constant pressure and thus map out the Gibbs energy surfaces.

We aim to answer the following questions:

(1) How many phases of pasta could coexist at a given depth in the crust?
(2) How does the structure of the energy surfaces evolve with depth?
(3) What is the characteristic temperature below which pasta could be locked into microscopic domains?
(4) What are the characteristic length scales of the domains?

In Sec. II we describe the numerical method. In Sec. III we describe our results, starting with a detailed description of our analysis of one particular layer, then displaying the rest of our results layer-by-layer. In Sec. IV we analyze what our results imply for the deep layers of the neutron star crust, and in Sec. V we give out conclusions.

II. NUMERICAL METHOD

There are many detailed accounts of the Skyrme-Hartree-Fock method [56], and we have outlined the method used in our previous paper [20]. Here we highlight details of the implementation that are important for this study.

A. Skyrme Hartree-Fock

Approximating the ground-state many-body wave function as a Slater determinant Φ, and minimizing the Skyrme energy density functional $\mathcal{E}_{\text{Skyrme}}[\Phi] = \langle\Phi|\hat{H}_{\text{Skyrme}}|\Phi\rangle$ with respect to the single-particle wave functions obtains the Skyrme Hartree-Fock equations. We write them with the inclusion of a quadrupole constraining potential, explained below, as

$$\left[-\nabla \frac{\hbar^2}{2m_q^*}\nabla + u_q(\mathbf{r}) + \lambda_c Q \right]\phi_{i,q}(\mathbf{r}) = \epsilon_{i,q}\phi_{i,q}(\mathbf{r}). \quad (1)$$

where $q = $ p,n label the isospin states, i the single-particle states. u_q are the one-body Hartree-Fock potentials,

$$
\begin{aligned}
u_q &= t_0\left(1 + \frac{1}{2}x_0\right)\rho - t_0\left(\frac{1}{2} + x_0\right)\rho_q \\
&+ \frac{1}{12}t_3\rho^\alpha\left[(2+\alpha)\left(1 + \frac{1}{2}x_3\right)\rho - 2\left(\frac{1}{2} + x_3\right)\rho_q\right.\\
&\left. -\alpha\left(\frac{1}{2} + x_3\right)\frac{\rho_p^2 + \rho_n^2}{\rho}\right] \\
&+ \frac{1}{4}\left[t_1\left(1 + \frac{1}{2}x_1\right) + t_2\left(1 + \frac{1}{2}x_2\right)\right]\tau \\
&- \frac{1}{4}\left[t_1\left(\frac{1}{2} + x_1\right) - t_2\left(\frac{1}{2} + x_2\right)\right]\tau_q \\
&- \frac{1}{8}\left[3t_1\left(1 + \frac{1}{2}x_1\right) - t_2\left(1 + \frac{1}{2}x_2\right)\right]\nabla^2\rho \\
&+ \frac{1}{8}\left[3t_1\left(\frac{1}{2} + x_1\right) + t_2\left(\frac{1}{2} + x_2\right)\right]\nabla^2\rho_q,
\end{aligned}
$$

and m_q^* is the effective mass,

$$
\begin{aligned}
\frac{\hbar^2}{2m_q^*} &= \frac{\hbar^2}{2m_q} + \frac{1}{4}\left[t_1\left(1 + \frac{1}{2}x_1\right) + t_2\left(1 + \frac{1}{2}x_2\right)\right]\rho \\
&- \frac{1}{4}\left[t_1\left(\frac{1}{2} + x_1\right) - t_2\left(\frac{1}{2} + x_2\right)\right]\rho_q. \quad (2)
\end{aligned}
$$

Here t_i, x_i, and α are parameters of the Skyrme interaction (for which we use the NRAPR parametrization [57]), $\rho = \rho_p + \rho_n$ are the nucleon densities and $\tau = \tau_p + \tau_n$ are the kinetic energy densities.

A key feature of our simulations is the quadrupole potential term we have added to the single-particle Hamiltonian $\lambda_c Q$ to control the geometry of the nucleon density distribution so we can systematically survey the shape space of the pasta configurations. The quadrupole operator has elements in coordinate space

$$Q_{ab} = 3x_a x_b - r^2\delta_{ab}, \quad (3)$$

with $\{x_a\} = x, y, z$.

Restricting ourselves to triaxial shapes, the quadrupole operator becomes diagonal $Q_a = 3x_a^2 - r^2$. The strength of the constraining force has components $\lambda_{c,a}$. This is an artificial potential whose strength is reduced to zero as we approach convergence, so that it does not give an artificial contribution to the total energy [58].

B. The computational grid

We solve the Hartree-Fock equations in coordinate space. The computational domain is taken to be a cube defined by Cartesian coordinates x_a with the origin at the centre of the cell. Each coordinate runs over $-l_a \leqslant x_a \leqslant l_a$, so that the length of the cell in each direction is $2l_a$. The space is discretized to form a grid of collocation points $x_{a,i}$ with even spacings in each direction Δx_a, defined by

$$x_a = \left(i + \tfrac{1}{2}\right)\Delta x_a, \quad i = -N_a, -N_a + 1, ...N_a - 1, \quad (4)$$

where N_a is the number of collocation points we use in direction a. In this work we use cubic cells so $N_x = N_y = N_z = N$. To make a large set of calculations feasible, we take parity in all three directions to be a good quantum number. It is thus sufficient to calculate just one octant of the computational cell. This means we limit ourselves to surveying triaxial shapes only. This means that certain topologically distinct phases (such as the gyroid) will be omitted,

$$\phi_{i,q}(\mathbf{r} + \mathbf{T}) = \phi_{i,q}(\mathbf{r}), \quad (5)$$

where $\mathbf{T}$ is the translation vector from the position $\mathbf{r}$ to the equivalent positions in the adjacent cells. The boundary conditions are enforced by representing the derivatives and solving for the Coulomb potential in Fourier space. The Coulomb solver is implemented using the FFTW software package [59]. Integrals on the grid are performed using the trapezoidal rule which is exact for functions represented by Fourier series [60].

The restrictions we impose above on our computational space are necessary for the large survey of densities, proton fractions and nuclear shapes to be tractable. They impose limitations noted below.

(i) We do not include the spin-orbit potential. This has the added benefit of the wave functions being entirely real functions and therefore reducing the computational cost. Although the spin-orbit interaction is important in determining the details of the energy spectrum in finite nuclei, it has been shown to make a much smaller contribution under crust conditions at high density, especially for the unbound neutron gas [61]. The spin-orbit interaction is thus not included in our simulations at present.

(ii) Enforcing simple periodic boundary conditions rather than the full Bloch boundary conditions makes the simulations susceptible to spurious shell effects [26]. These arise in large part from the artificial discretization of the unbound neutrons' single-particle spectrum caused by restricting the calculations to a finite volume. This makes comparing results at different cell sizes unreliable as in low proton fraction matter the variation of the spurious contribution to the shell energy is of similar magnitude to the physical contribution, and consequently we cannot find the energetically preferred unit cell size. We will therefore restrict ourselves to probing the shape of nuclear configurations at constant cell sizes.

C. Single-particle states

Our solution to the Hartree-Fock equations begins with an initial guess for the wave functions. We have found that starting the neutron wave functions as plane waves and the proton wave functions as harmonic oscillator wave functions leads to most efficient convergence; other combinations of initial wave functions were tested, and it was verified that they lead reliably to the same ground state configurations so long as we impose the quadrupole constraint to control the shape of the configuration. The number of possible single-particle states we can represent on our grid is $(N-1)^3$, and we evolve all of them; those that start out unoccupied often evolve to be occupied in the converged final state.

We impose BCS pairing, so that single-particle states are occupied according to the distribution function

$$w_{k,q}^{\text{pair}} = \frac{1}{2}\left(1 - \frac{\epsilon_{k,q} - \epsilon_{F,q}}{\sqrt{(\epsilon_{k,q} - \epsilon_{F,q})^2 + f_{k,q}^2 \Delta_q^2}}\right), \qquad (6)$$

where $f_{k,q}$ is a function that acts to cutoff coupling to continuum states and confine the active pairing space to the vicinity of the Fermi surface [62]. The pairing gap Δ_q is taken to be a constant, set as $\Delta_q = 11.2\,\text{MeV}/\sqrt{A}$ [63]. Other than the fact that pairing is a physical feature of our system, it significantly improves convergence of our iterations.

D. Iterative solution

We solve the HF equations iteratively, forming densities and potentials from the current wave functions and solving the HF equations to obtain new wave functions repeatedly until the wave functions converge. We combine two different algorithms to achieve the convergence to the ground state with maximum efficiency.

We start off using the imaginary time step iteration [64], an adaptation of the time-dependent HF iteration $\phi_{i,q}^{(n+1)} = e^{-i\hat{h}_{\text{HF}}^{(n+1/2)}\Delta t/\hbar}\phi_{i,q}^{(n)}$ which evolves the wave functions by a time interval Δt. Here, $\hat{h}_{\text{HF}}^{(n+1/2)}$ is a numerical approximation to the Hamiltonian at the half-time step $(n+1/2)\Delta t$. The imaginary time step is obtained by replacing Δt with $-i\Delta t$ and $\hat{h}_{\text{HF}}^{(n+1/2)}$ with $\hat{h}_{\text{HF}}^{(n)}$. Defining the parameter $\lambda = \Delta t/\hbar$, and expanding the exponential in a power series, the $(n+1)$th wave function is formed from the nth by

$$\phi_{i,q}^{(n+1)} = e^{-\lambda\hat{h}_{\text{HF}}^{(n)}}\phi_{i,q}^{(n)} = \sum_{k=1}^{k_{\text{cut}}} \frac{1}{k!}\left(-\lambda\hat{h}_{\text{HF}}^{(n)}\right)^k \phi_{i,q}^{(n)}, \qquad (7)$$

where λ controls the magnitude of the imaginary time step, that is the size of the iterative step. We can adjust the number of terms contained in the exponential expansion through k_{cut}.

The imaginary time step iteration is very robust - even if we start with a set of initial wave functions that are far from those of the ground state solution, it will remain stable. It converges quickly initially, but as one approaches convergence, it slows down exponentially. Thus, when we get closer to the ground state we switch to the damped gradient iteration [58,65]. Here,

the $(n+1)$th wave function is formed from the nth by

$$\phi_{i,q}^{(n+1)} = \phi_{i,q}^{(n)} - x_0\hat{D}(e_0)\left(\hat{h}_{\text{HF}}^{(n)} - \epsilon_{i,q}^{(n)}\right)\phi_{i,q}^{(n)}, \qquad (8)$$

where the damping operator

$$\hat{D} = \left[1 + \frac{\hat{t}_x}{e_0}\right]^{-1}\left[1 + \frac{\hat{t}_y}{e_0}\right]^{-1}\left[1 + \frac{\hat{t}_z}{e_0}\right]^{-1} \qquad (9)$$

acts to damp out large kinetic energy components of the wave functions with kinetic energies above e_0 that slow down convergence. Here $\hat{t}_a$ are the one-dimensional kinetic energy operators. The damped gradient iteration requires initial wave functions that are relatively close to the actual ground state wave functions; otherwise, it becomes unstable. It converges roughly linearly and so is more efficient than the imaginary time step at late times.

E. The quadrupole constraint

To systematically survey the spectrum of nuclear geometries and their corresponding energies, we need control the geometry of the ground state to which an iteration converges without excluding any of known pasta geometries. To do this we implement a quadrupole constraint. Given the reflection symmetry, the next order deformation, consistent with our boundary conditions, is hexadecapole. It is expected to give energy variations at least an order of magnitude smaller than that of the quadrupole deformation.

Taking the quadrupole operator to be diagonal, the quadrupole moments of the nucleon density distribution are the matrix elements

$$q_a = \langle\hat{Q}_a\rangle = \sum_{i=1}^{N}\langle\phi_i|Q_a|\phi_i\rangle. \qquad (10)$$

The three nonzero quadrupole moments must also fulfill $q_x + q_y + q_z = 0$, so just two of them are independent. The nuclear shape can be parameterized in Cartesian or spherical polar coordinates

$$\begin{aligned}
R &= R_0(1 + \alpha_x\xi^2 + \alpha_y\eta^2 + \alpha_z\zeta^2) \\
&= R_0[1 + \alpha_{20}Y_{20}(\theta,\phi) + \alpha_{2+2}Y_{2+2}(\theta,\phi) \\
&\quad + \alpha_{2-2}Y_{2-2}(\theta,\phi)],
\end{aligned} \qquad (11)$$

where $q_a = R_0\alpha_a$ for $\{a\} = x, y, z$, R_0 is the root-mean-square nuclear radius, $\xi = x/R_0$, $\eta = y/R_0$ and $\zeta = z/R_0$. The spherical polar moments are related to their Cartesian counterparts via

$$\alpha_{2\pm2} = \sqrt{\frac{2\pi}{15}}(\alpha_x - \alpha_y) \equiv \alpha_2, \qquad (12)$$

$$\alpha_{20} = \sqrt{\frac{8\pi}{90}}(2\alpha_z - \alpha_x - \alpha_y) \equiv \alpha_0, \qquad (13)$$

where α_0 is the relative stretch along the z axis of the nuclear cluster with respect to the x and y axes and α_2 is the relative difference in length between the x and y axes. We can define the parameters β, γ [66]:

$$\alpha_0 = \beta\cos\gamma, \quad \alpha_2 = \frac{1}{\sqrt{2}}\beta\sin\gamma, \qquad (14)$$

analogous to polar coordinates in (α_0, α_2) space: β represents the magnitude of the deformation of the configuration, and γ the direction of the deformation from prolate $\gamma = 0^o$ to oblate $\gamma = 60^o$.

We specify our desired quadrupole moments through the polar coordinates α, β given in Eq. (14). These are then turned into the moments q_a through Eqs. (12) and (13), the requirement that $\alpha_x + \alpha_y + \alpha_z = 0$ and the definition $q_a = R_0\alpha_a$.

The force strength needs to be updated iteration by iteration as it drives the quadrupole moments toward the desired values [58]. Denoting the quadrupole moments we wish our nuclear configuration to converge toward by $q_{a,0}$, the procedure is as follows: An intermediate iteration is carried out $|\tilde{\phi}_i^{(n)}\rangle = \mathcal{O}I[(\hat{h}_{HF} + x_0\lambda_c^{(n)} \cdot \hat{Q})|\phi_i^{(n)}\rangle]$, where I represents the operation of either the imaginary time step iteration or the damped gradient iteration, and x_0 is the same parameter that controls the damped gradient iteration step. Intermediate quantities $|\tilde{\phi}_i^{(n)}\rangle$, $\tilde{\rho}^{(n)}$, $\tilde{q}_a^{(n)}$, $\tilde{q}_a^{2\,(n)}$ are calculated. The components of the constraining force strength are updated at each step according to

$$\lambda_{c,a}^{(n+1)} = \lambda_{c,a}^{(n)} + \frac{c_0(\tilde{q}_a^{(n)} - q_a^{(n)})}{2x_0(q_a^{2\,(n)} - (q_a^{(n)})^2/N_q) + d_0}, \tag{15}$$

where N_q is the number of particles of species q. We define

$$\delta\lambda_{c,a} = \frac{c_0(q_a^{(n)} - q_{a,0})}{2x_0(q_a^{2\,(n)} - (q_a^{(n)})^2/N_q) + d_0}. \tag{16}$$

Finally, the $(n + 1)$th wave functions are formed as $|\phi_i^{(n+1)}\rangle = \mathcal{O}[(|\tilde{\phi}_i^{(n)}\rangle - x_0(\lambda_c^{(n+1)} - \lambda_c^{(n)} + \delta\lambda_c)\hat{Q})|\tilde{\phi}_i^{(n)}\rangle]$ from which we finally obtain the updated quantities. Here, c_0 and d_0 are parameters adjusted for optimum convergence of the constraint iteration. This procedure must be performed for the three components of the quadrupole moment $a \in \{x, y, z\}$. Note that as we converge to the ground state with the desired quadrupole moments, the strength of the constraining force tends to zero.

We apply the constraint only to the neutrons; test simulations show that the proton density distribution follows the neutron density distribution to a good degree of accuracy [67]. It is important to note that the constraint itself does not bias us; as we shall see, the constraint phase space we explore admits all triaxially symmetric pasta shapes, and by systematically exploring that space we allow for the appearance of all possible shapes.

F. Numerical parameters and testing

The simulations were conducted with the following parameter values. The imaginary time step iteration had a step size of $\lambda = 5 \times 10^{-4}$ and a cutoff in the exponential at 5th order. The damped gradient iteration has a step size of $x_0 = 0.4$ and kinetic energy cutoff of 40 MeV. The quadrupole iteration has parameters $c_0 = 0.03$, $d_0 = 0.9$.

Convergence is achieved when the sum of the variance over all the wave functions $\sum_i w_{i,q}[\langle\phi_{i,q}|h_{HF}^2|\phi_{i,q}\rangle - (\langle\phi_{i,q}|h_{HF}|\phi_{i,q}\rangle)^2]$ drops below 1 keV^2, which generally corresponds to convergence in the total energy of order 1 part in 10^8 or better. It takes of order 1 000–10 000 iterations per
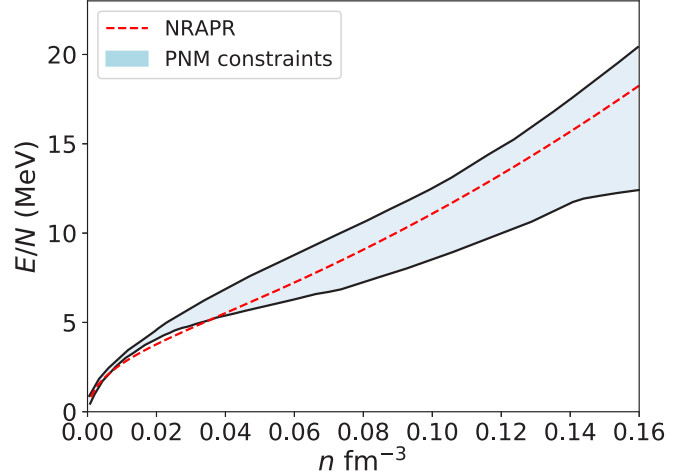

FIG. 1. The pure neutron matter EOS of the NRAPR Skyrme parametrization used in this work (red dashed line) compared to the region predicted by *ab initio* calculations of PNM [70–72]. Given the importance of the PNM EOS to crust properties, it is important to consider the consistency of the interaction used to model the crust and our best theoretical knowledge of PNM.

run to achieve this convergence, corresponding to run times of 1–10 h.

The code was comprehensively tested and validated as outlined in Ref. [20]. It was established that the optimal grid spacing (the compromise between accuracy and computation time) is 1.2–1.3 fm, which we use here. We established that the periodic boundary conditions have a 1 part in 10^4 effect on the total energy of the cell, and that the nuclear shapes we obtain are not artifacts of the finite cell size (the same nuclear shapes are obtained when we double the cell size in in each direction).

G. Nuclear interaction used

The pressure, and hence stability, of the inner crust is provided by the fluid of dripped neutrons in which the lattice of nuclei and nuclear pasta is immersed. *Ab initio* pure neutron matter (PNM) calculations are therefore an important guide for neutron star EOSs [68,69]. In our investigation, it is important to choose a nuclear model that predicts a pure neutron matter EoS consistent with these calculations. We choose the NRAPR parametrization of the Skyrme interaction [57], which is fit to the APR neutron matter EOS. It gives a slope of the symmetry energy of $L = 60$ MeV, which is of intermediate stiffness. Figure 1(a) shows the NRAPR EOS and the band from recent *ab initio* calculations of the PNM matter EOS [70–72]. The extent of the pasta phases is sensitive to the EOS, particularly the symmetry energy parameters of nuclear matter; a follow-up study will examine the dependence of our results on the EOS. Preliminary results suggest the results are qualitatively similar.

H. Choosing the cell size and proton fraction

It is currently computationally prohibitive to conduct a full minimization over cell size. The presence of spurious shell
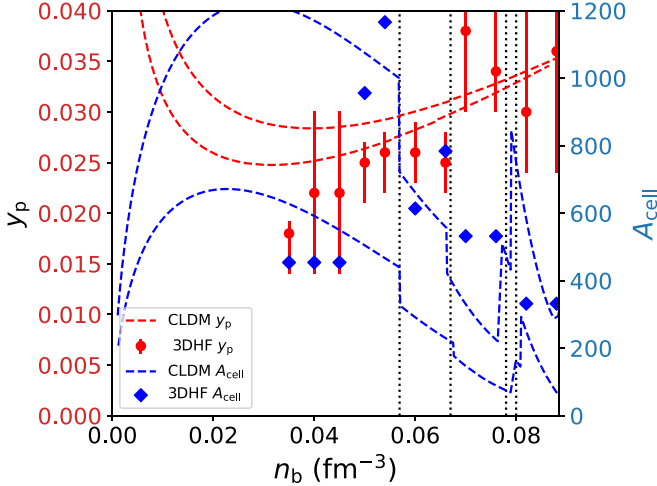
FIG. 2. The red and blue dashed lines are the bounds of the total nucleon number in the cell A_{cell} and the average proton fraction y_p from a compressible liquid drop model using the NRAPR interaction [57] and varying the surface energy parameters over a reasonable range [73]. Vertical dotted lines indicate the transition to cylindrical nuclear pasta, slabs, cylindrical holes and spherical holes with increasing density. The transitions are accompanied by discontinuities in the cell size. The blue diamonds are the values of A_{cell} we choose to perform our 3DHF calculations at. The red points indicate the β-equilibrium proton fractions we at each density from our 3DHF calculations, and the "error bars" through them indicate the range of proton fractions we performed calculations at.

effects make such a minimization unreliable, and in future a consistent minimization should be done using methods that minimize spurious shell effects, such as the use of twist-averaged boundary conditions [26].

Instead, we choose to conduct the calculations at cell sizes and proton fractions guided by the compressible liquid-drop model (CLDM) [73]. We have checked the proton fractions corresponding to β equilibrium for both the 3DHF model and CLDM, and they agree well. In Fig. 2 we show the predictions of the proton fraction y_p and total nucleon number in the unit cell A_{cell} from the CLDM varying the surface energy of the CLDM over a wide range, together with total nucleon numbers A_{cell} and range of proton fractions we choose to perform calculations at in this work. The total nucleon number characterizes the cell size at a given baryon density n_b, since the computational volume we use is calculated as $V = A/n_b$. Our choice of A_{cell} as a function of density follows the rough trend predicted by the CLDM.

At each density, we perform calculations at two to three of values of A_{cell} to assess the A_{cell} dependence of our results. We find no qualitative dependence of our results on A_{cell}, so will present our results for a single representative cell size. We also calculate a number of different proton fractions to make sure we can locate β equilibrium within our quantum simulation: the variations with y_p will be explicitly presented. The range of proton fractions covered are indicated by the bars on the proton fraction points in Fig. 2.

III. RESULTS

We perform around 500 000 CPU h of 3DHF+BCS calculations. To give a detailed example of our methods, we will first present an analysis of the layer of pasta at a baryon number density of around $n_b = 0.06\,\text{fm}^{-3}$. We will then move to lower and higher densities to examine the layers where pasta first emerges and finally transitions to uniform matter, before summarizing results across the whole pasta region.

A. A case study: $n_b \approx 0.06\,\text{fm}^{-3}$

We begin our investigation by calculating the minimum energy configurations at a constant cell size corresponding to a total nucleon number of $A_{cell} = 614$, which is in the range predicted by the CLDM calculations. We perform calculations over a range of deformation parameters: the full range of γ from prolate configurations $\gamma = 0°$ to oblate configurations $\gamma = 60°$ with a step of $\Delta\gamma = 5°$, and for a range of magnitudes of deformation β that cover all unique local minima, which at this density ranges up to $\beta = 0.24$. We use a step size of $\Delta\beta = 0.03$. We perform these calculations at a range of different values of the proton fraction to locate the β-equilibrium value. The results are shown for the three values of y_p around β equilibrium: $y_p = 0.023$, 0.026, and 0.029 (corresponding to proton numbers of $Z = 14$, 16, and 18).

In Fig. 3 we show the resulting energy surfaces as a function of deformation (β, γ). The energy per baryon is plotted versus the magnitude β and direction γ of the deformation. The most important feature is that there are *multiple* local minima in all three energy surfaces, visible as the darker blue regions. There are minima located in broadly the same regions of deformation space for each proton fraction: at small deformations in the intermediate to oblate sense ($\beta = 0.03$–0.06, $\gamma \approx 30$–60°), at stronger prolate deformations ($\beta = 0.12$–0.18, $\gamma = 0$–25°) and high deformations in the oblate direction ($\beta = 0.15$–0.21, $\gamma = 50$–60°). The lowest energies occur for the proton fraction of $y_p = 0.26$. However, the energy separation of local minima is small and there is no obviously pronounced ground state. This initial calculation confirms a number of other microscopic studies that have shown that matter deep in the crust is frustrated, and might have an amorphous, heterogeneous structure characterized by many local energy minima [16]. The next order deformation consistent with the symmetry of the unit cell used, hexadecapole, is expected to give energy variations an order of magnitude smaller than those of the quadrupole deformation. However, we should be aware that the particular pasta phase found at a given (β, γ) point is unlikely to be unique: different pasta phases with the same (β, γ) but different higher order moments could exist.

It is worth thinking about how matter with this structure will behave as the crust of the neutron star cools. Different local regions of a given layer inside the star will fall into different local minima, and when the temperature falls below some critical value associated with the energy barriers between minima they will be trapped in those minima for some
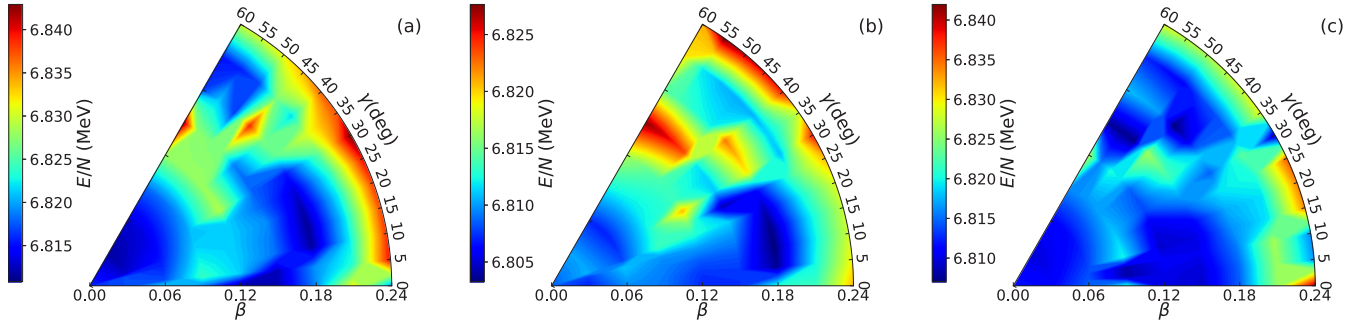
FIG. 3. Energy-deformation surfaces at an average density of $n_b = 0.06\,\text{fm}^{-3}$ for cells containing $A_{\text{cell}} = 614$ nucleons and a proton fraction of 0.023 (a), 0.026 (b), and 0.029 (c). Many local minima (dark blue troughs) appear in the landscapes; the pasta configurations appearing in those minima can be seen in Fig. 5.

quantum tunneling timescale (which is likely to be related to the very uncertain pycnonuclear fusion timescale of heavy nuclei just above the pasta layers). On longer timescales, the crust might be able to anneal and eventually all the pasta at a given density could be converted into the ground state configuration. Depending on the temperature scales set by the energy barriers between local minima, crustal heating later in the neutron star's life might repopulate the local minima. Thus, the pasta layers might plausibly transition between a single pasta configuration and multiple coexisting pasta configurations at different stages in the star's life.

Here we explore the possibility that different phases corresponding to the local minima coexist in microscopic domains, at a given depth in the crust. Such domains would exist in equilibrium at constant pressure; however, the calculations we perform are at constant density rather than constant pressure. To determine the local minima that will coexist, we need to calculate the Gibbs free energy at constant pressure as a function of β and γ.

To do this, we perform calculations of the energy surfaces over a range of densities in the range $n_b = 0.058\,\text{fm}^{-3}$– $0.062\,\text{fm}^{-3}$. We pick a reference pressure, which we choose to be that of the zero-deformation configuration $(\beta, \gamma) = (0, 0°)$, at $n_b = 0.06\,\text{fm}^{-3}$: $P_{\text{ref}} = 0.291\,\text{MeV fm}^{-3}$. We then use interpolation to find the density at which the pressure is equal to the reference pressure for all other deformation values, and the energy at that density. We then calculate the specific Gibbs free energy $G = E + P/n_b$. The interpolations assume there is no discontinuous change in energy with density at a particular point in deformation space, which would be associated with a change of shape. This cannot be guaranteed, but so long as the interpolation window is small and we use a sufficiently large number of points in deformation space, we can reasonably assume it will occur infrequently enough that it will not affect the global features of the energy surface. Such discontinuities would show up as artifacts in the energy surfaces, and we see no such features.

In Figs. 4(a)–4(c) we show the Gibbs free-energy surfaces at constant pressure in deformation space at the three values of the proton fraction, and in Figs. 4(d)–4(f) we show the corresponding density variations over each surface. In all three cases, local minima appear at broadly the same locations as we found in the internal energy surface at constant density

n_b. The range of average baryon density is smaller than the range over which we performed the interpolations, indicating the interpolations are robust. Domains in different regions of deformation space will have different average baryon densities, so if they coexist at a given density in the crust, there will be fluctuations in density of order $10^{-3}\,\text{fm}^{-3}$, or $\Delta n_b/n_b \sim 1\%$ of the total density. These fluctuations will have length scales corresponding to the size of the domains, which we will estimate shortly. The three regions where minima occur are large oblate deformations (higher density), small intermediate deformations (intermediate density), and intermediate prolate deformations (lower density).

Local minima in the Gibbs energy surfaces are separated by energy barriers. To more clearly see the relative height of the barriers and the difference in energy between local minima, we now plot the energy along one-dimensional paths across the deformation landscapes. We choose plots that link local minima by continuous deformation and require traversing the smallest energy barriers possible. The top of Fig. 5 shows the Gibbs energy surfaces from Fig. 4 with the paths marked. The central plot on Fig. 5 shows the Gibbs energy along those paths. To orient the reader, the directions marked by the arrows on the surface plots show the direction moving left to right in the main plot of the one-dimensional trajectories. We also show selected values of the deformation coordinates (β, γ) along the one dimensional trajectories.

The plot of the energy along the trajectories shows that indeed the Gibbs energy is on average lowest for the proton fraction of $y_p = 0.026$. However, two minima at a proton fraction $y_p = 0.029$ have smaller Gibbs energies than some local minima at $y_p = 0.026$. There may be a local variation of average proton fraction (and hence electron density) from domain to domain.

We have circled the six lowest local minima. All other local minima can access these six local minima by continuous deformation and adjusting their proton fraction through β decay and electron capture without having to pass over an energy barrier. For example, matter at the local minimum at $y_p = 0.29$, $(\beta, \gamma) \approx (0.06, 60°)$ can reach the minimum at $y_p = 0.26$, $(\beta, \gamma) \approx (0.06, 60°)$ through electron capture.

The pasta configurations corresponding to each of the 6 minima are revealed by plotting surfaces of constant neutron density in our unit cell. These are shown in the six plots under
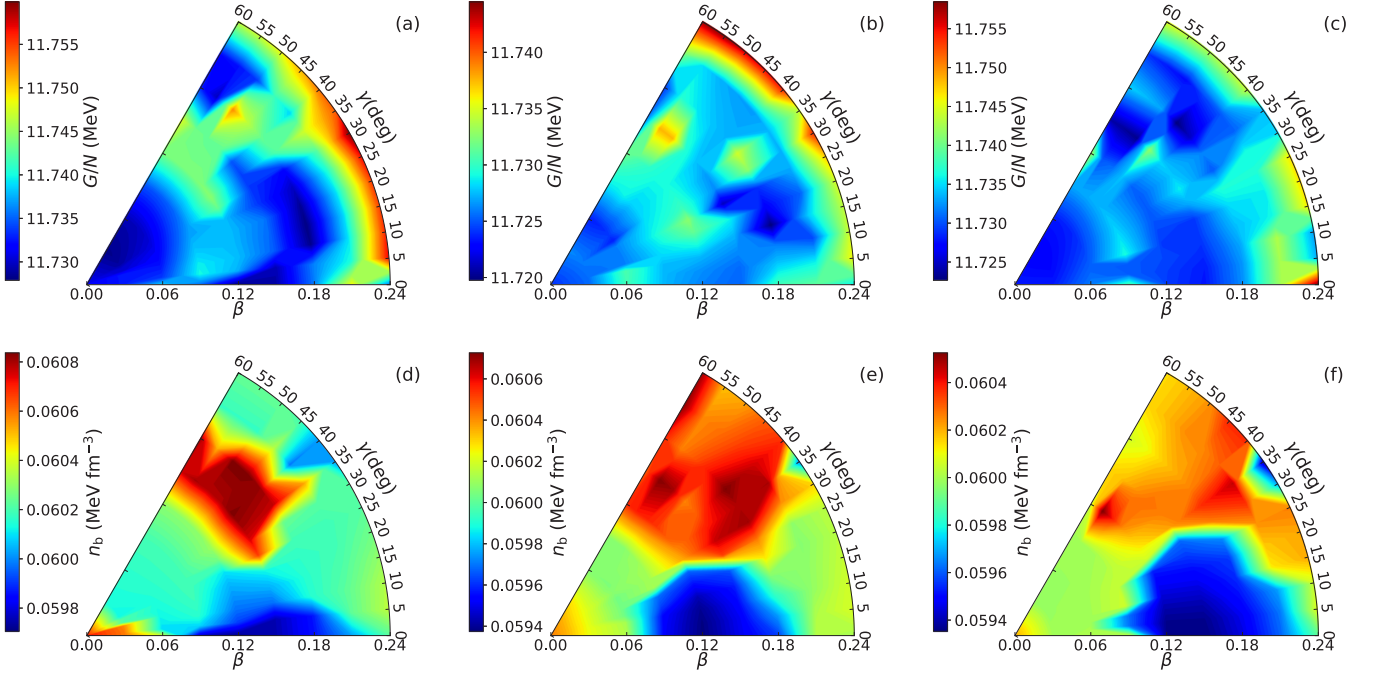
FIG. 4. Gibbs energy-deformation surfaces (a)–(c) and average baryon density surfaces (d)–(f) at a constant pressure of 0.291 MeV fm^{-3} for cells containing $A_{\text{cell}} = 614$ nucleons. Results are shown for proton fraction of 0.023 (a), d), 0.026 (b), (e), and 0.029 (c), (f). The local minima differ in baryon density by of order 5%. The pasta configurations appearing in those minima can be seen in Fig. 5.

the one dimensional energy plot. The neutron density at which to plot these surfaces is chosen to be the average neutron density $n_{\text{b}}(1 - y_{\text{p}})$. The following pasta configurations are found:

(i) $y_{\text{p}} = 0.026$, $(\beta, \gamma) = (0.18, 60°)$—the nuclear waffle phase (the "hole" of the waffle is centered on the edge of each cell).

(ii) $y_{\text{p}} = 0.026$, $(\beta, \gamma) = (0.15, 25°)$—the nuclear spaghetti phase.

(iii) $y_{\text{p}} = 0.026$, $(\beta, \gamma) = (0.18, 15°)$—another form of nuclear waffle; large spherical nuclei with bridges connecting to adjacent cells in two different directions. The nucleus is centered on the y boundary of the computational volume.

(iv) $y_{\text{p}} = 0.026$, $(\beta, \gamma) = (0.06, 15°)$—similar to the previous configuration, a deformed nucleus with bridges to adjacent cells. The nucleus is now centered in the computational volume.

(v) $y_{\text{p}} = 0.029$, $(\beta, \gamma) = (0.18, 45°)$—the nuclear waffle phase.

(vi) $y_{\text{p}} = 0.029$, $(\beta, \gamma) = (0.18, 45°)$—nuclear waffle phase (like the waffle configuration at $y_{\text{p}} = 0.026$, the "hole" of the waffle is centered on the edge of each cell).

The detailed structure of the minima is dependent on the nuclear interaction used and the total cell size. However, a precise extraction of the relative energy differences of minima and the barrier heights is not merited, as it is extremely unlikely that those details will ever be accessible through observational data. Hence, instead of using the exact values of the energies of all six minima and the barriers between them,

we create a slightly simpler model based on these results. The model is depicted schematically in Fig. 6. We first reduce the number of minima from six to four, representing the four distinct configurations present. The two forms of nuclear waffle are distinct enough that we include them as separate configurations, though they may not give rise to any observable differences). The $y_{\text{p}} = 0.026$, $(\beta, \gamma) = (0.06, 15°)$ and $(0.18, 15°)$ minima are essentially the same, so we take the lowest of those two minima and ignore the other one (which, being the highest lying of the minima, will be least populated). Also, we treat the two waffle phases at $y_{\text{p}} = 0.029$ as a single minimum. Although these are similar to the waffle phase at $y_{\text{p}} = 0.026$, the different proton fractions makes them physically distinct. Finally, we make the simplification that there is just one single characteristic barrier height between phases, G_{barrier}, taken to be the average of all the barriers between minima.

The four minima are represented schematically in Fig. 6. Under each minima we plot the neutron surfaces again for stacks of 4×4 unit cells of matter, to better see the structure of matter at larger scales (but note that the computation is done only in one unit cell). We have four distinct phases: the ground state is the waffle phase consisting of large nuclei connected to adjacent cells in two directions. The next lowest lying minimum is the spaghetti phase. Then the next two are nuclear waffle phases—intermediate phases between spaghetti and lasagna—at two different proton fractions.

To characterize the properties of these possibly amorphous phases of matter, we borrow a concept from the study of terrestrial amorphous materials. An effective or "fictive" temperature, T_{f} [74] is defined as the temperature from which, if the material was instantaneously quenched to
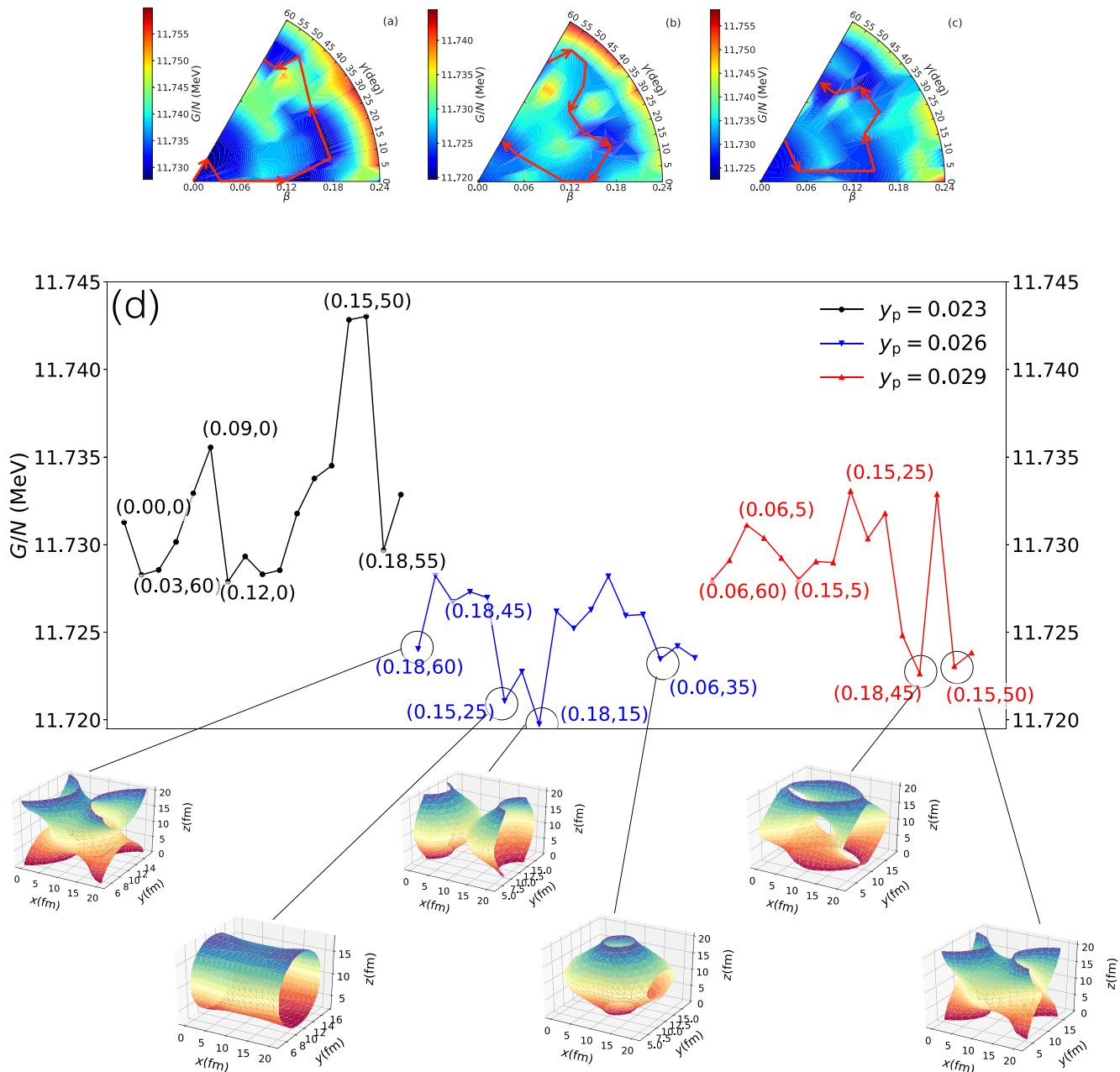
FIG. 5. The top row (a)–(c) shows the Gibbs free-energy surfaces from Fig. 4 at a constant pressure of 0.291 MeV fm^{-3} (densities around 0.06 fm^{-3}) with red arrows indicating paths between local minima that pass over the smallest energy barriers. Underneath is the corresponding one-dimensional plot of the Gibbs energy along those paths (d). Selected (β, γ) coordinates are shown along the one-dimensional plots. 3D surfaces at constant neutron density in the cell show the shape of the nuclear cluster in the cell at the local minima indicated. The other apparent local minima can transition exothermically to one of the highlighted minima by β decay or electron capture.

zero temperature, or any other temperature $T < T_{\rm f}$, its state would be that of the material at a temperature $T_{\rm f}$ (no reconfiguration of its microscopic degrees of freedom would occur). In our context, the fictive temperature is the temperature equivalent to the energy barrier height between minima. As the temperature falls below $T_{\rm f}$, thermal fluctuations can no longer rearrange matter, and so *in the absence of quantum tunneling between the barriers* the matter is frozen into the state at $T_{\rm f}$. Of course, quantum tunneling will occur, but the timescales over which that would occur and rearrange potentially large regions

of nuclear pasta are not well known (the closest timescales from the literature would be pycnonuclear fusion timescales, but as we shall see whole domains of nuclei need to be rearranged for matter to substantially change its structure at the mesoscopic level.

In this work, as illustration of the concept and derive some order-of-magnitude implications, we choose the fictive temperature to be the height of the highest energy barrier relative to the lowest lying minimum, indicated as $T_{\rm f}$ in Fig. 6.
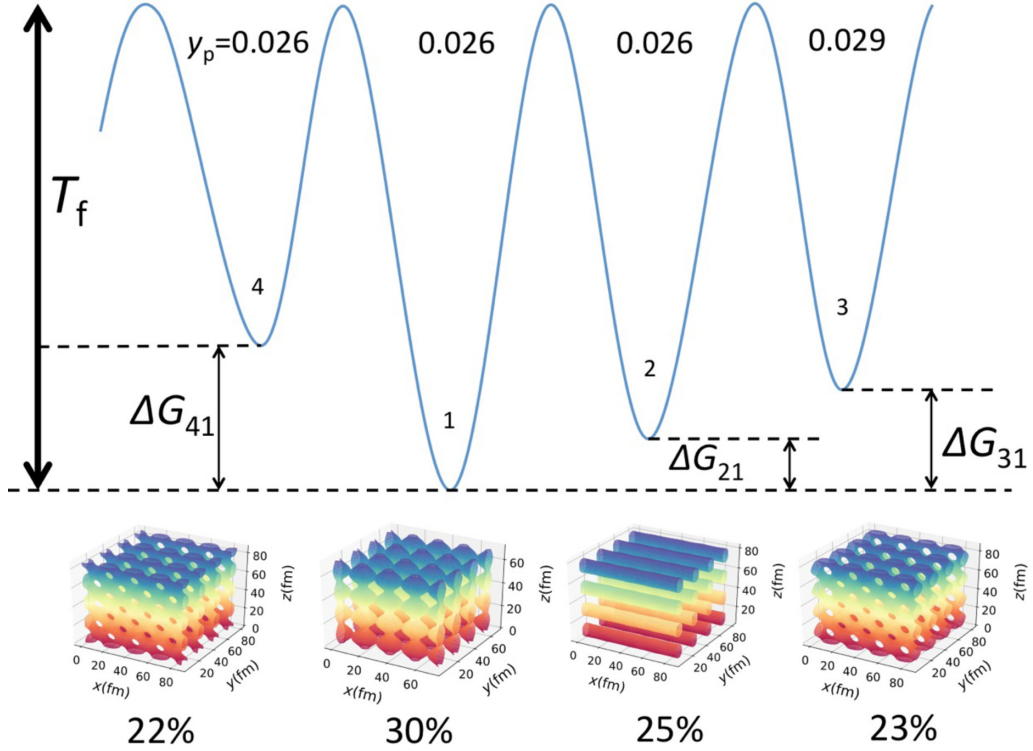
FIG. 6. Illustration of our schematic model for pasta domains in local Gibbs energy minima at densities around $0.06\,\text{fm}^{-3}$ where calculations present four physically distinct local minima. To visualize the phases better we have plotted a region of four by four unit cells, but it is important to remember we only simulate one single unit cell. The proton fractions corresponding to the minima we found are shown above each minima. The fictive temperature T_f is given by the height of the energy barriers, and the energy differences between he local minima are indicated as ΔG The relative abundances of the phases at a temperature equal to the fictive temperature is shown below the visualizations of the phases. In the simplified model we take a single barrier height to be the fictive temperature. This is determined as the average of the various barriers in our calculation. These abundances will be frozen in as the temperature drops further unless processes such as quantum tunneling anneal the matter.

The ratio of the abundance of the pasta in the *i*th minimum to the *j*th minimum is given by

$$\frac{N_\text{i}(T_\text{f})}{N_\text{j}(T_\text{f})} = e^{\Delta G_{\text{ij}}/kT_\text{f}}, \tag{17}$$

where $\Delta G_\text{ij} = G_\text{i} - G_\text{j}$. Given that the occupation probability for minimum i is given by $p_i = N_i / \sum_j N_j$ and $\sum_i p_i = 1$, then the occupation probability of a particular minimum j can be written

$$p_\text{i}(T_\text{f}) = \frac{e^{\Delta G_{\text{i0}}/kT_\text{f}}}{1 + \sum_{j \neq 0} e^{\Delta G_{\text{j0}}/kT_\text{f}}}. \tag{18}$$

Based on Eq. (18), the abundances of pasta in each of the four phases in our simplified model in Fig. 6 are shown as the percentages under the visualizations of the pasta.

Let us assume, to obtain a lower limit on the fictive temperature below which the pasta becomes frozen-in to the local minima, that the nucleons behave as free quasiparticles, Then differences in the energy *per particle* between local minima and the energy barriers that separate them set the temperature scale required to transition from one pasta structure to another through thermal fluctuations. Realistically, this temperature scale will be modified upwards by a factor taking into account the extent to which the nucleons in the pasta and free neutron

gas behave collectively during the rearrangement from one phase to another. A more accurate picture might suppose that a number of nucleons in the unit cell of order the proton number act collectively in the transition between phases, since the main driver of the shape formation is the electrostatic lattice energy. This number may also be modified by the number of unbound neutrons entrained by the cluster [75]. Typically, this accounts for $\sim$10% of the nucleons and so our lower limit could underestimate the fictive temperature by a factor of $\sim$10. To account for this factor, we can multiply the temperature by a factor $A_\text{collective}$ which accounts for the number of nucleons in the unit cell that act collectively, and then $kT_\text{f} = A_\text{collective} G_\text{barrier}$. Note that the number of nucleons per unit cell that behave collectively upon shape rearrangement does not affect the equilibrium distribution, since both the energy difference between minima and the fictive temperature scale by $A_\text{collective}$.

For pasta geometries continuous in one or more dimensions like spaghetti and lasagna, the unit cell does not have a physical meaning in that direction, but, for example, a transition between spaghetti and waffle phases requires the creation of connecting arms perpendicular to the spaghetti axis which are periodic according the unit cell size. Therefore, the unit cell is still the relevant unit of matter when we think about rearranging nuclear pasta.

In our simplified model, the fictive temperature is taken to be the average height of the barriers relative to the lowest minimum along the one-dimensional trajectories at $y_p = 0.026$ and $y_p = 0.029$ in Fig. 5: $kT_f = 7.7\,\mathrm{keV} \rightarrow T_f = 8.9 \times 10^7\,\mathrm{K}$ ($T_8 = 0.89$ where $T_8 = T_f/10^8\,\mathrm{K}$). Minima 1 and 2 are separated by energies $\Delta G_{21} = 1.6\,\mathrm{keV}$/particle, minima 1 and 3 by $\Delta G_{31} = 2.0$ keV/particle and minima 1 and 4 by $\Delta G_{31} = 2.4$ keV/particle.

At temperatures below 8.9×10^7 K the composition of the domains will be frozen with respect to thermal fluctuations for a timescale that depends on the poorly known tunneling timescale (but which could be short compared to the cooling timescale). The relative abundance of the pasta phases corresponding to the four minima is 0.30:0.25:0.23:0.22, respectively (see Fig. 6). Thus, about 70% of the composition of this layer is at a proton fraction 0.026 and 30% is at a proton fraction 0.029. We can thus expect fluctuations in average proton (and, correspondingly, electron) fraction at the microscopic level at the level of around 10%. Also around 75% of matter is in wafflelike configurations, and 25% is in the spaghetti configuration.

1. The size of domains

The scale on which the pasta phases are ordered can be found by estimating the length L over which thermal fluctuations disrupt the long-range order of spaghettilike and lasagnalike configurations. Since the waffle phases are planar, they can be approximated here as lasagna phases. We follow the formalism laid out in Ref. [51]. Relative to the cell spacing $d = 2r_c$ where r_c is the cell radius, it is given as follows:

For the spaghettilike structures,

$$\left(\frac{L}{d}\right)_{\mathrm{spaghetti}} \approx \left[\frac{(B_{2d} + 2C_{2d})(\pi\lambda a)^{1/2}}{k_B T}\right]^{1/2}, \quad (19)$$

where

$$B_{2d} = 1.5 w_{C+L} \quad C_{2d} \approx 10^{2.1(u-0.3)} w_{C+L}, \quad (20)$$

$$K_3 \approx 0.0655 w_{C+L} r_c^2 \quad a \approx 2r_c. \quad (21)$$

For 1D lasagnalike structures,

$$\left(\frac{L}{d}\right)_{\mathrm{lasagna}} \approx \left[\frac{4\pi(BK_1)^{1/2}}{k_B T \ln\left(\frac{R}{2r_c}\right)}\right]^{1/2}, \quad (22)$$

where

$$B_{1d} = 6 w_{C+L}, \quad K_1 \approx \tfrac{2}{15} w_{C+L}(1 + 2u - 2u^2) r_c^2, \quad (23)$$

and R is the typical length of the structure, u the volume fraction of the pasta. w_{C+L} is the total electrostatic energy density, including the all important lattice contribution which, in addition to quantum shell effects, drives the stability of the phases. The electrostatic energy density w_{C+L} is extracted from the simulation. The factors involving u change only by a factor of at most 2 over a reasonable range of u (as they enter as powers of 1/4), so for simplicity and since we are interested only in a rough estimate of length scales, we take the average of that range and fold it into the numerical prefactor.

At low temperatures $<10^7$K, this overestimates the order, because quantum fluctuations become important, but our

lower limits on the fictive temperature are all significantly above 10^7K.

The electrostatic energy per nucleon is $W_{C+L} = V w_{C+L}/A$ where V is the volume of the cell and A_{cell} the number of nucleons in the cell. $V = r_c^3$, and using $kT_f = A_{\mathrm{collective}} G_{\mathrm{barrier}}$ and evaluating the numerical factors,

$$\left(\frac{L}{d}\right)_{\mathrm{spaghetti}} \approx \left(\frac{r_c - r_N}{r_c}\right)\left(\frac{A_{\mathrm{cell}}}{A_{\mathrm{collective}}}\right)^{1/2}\left(\frac{W_{C+L}}{G_{\mathrm{barrier}}}\right)^{1/2} \quad (24)$$

and

$$\left(\frac{L}{d}\right)_{\mathrm{lasagna}} \approx \left(\frac{L}{d}\right)_{\mathrm{spaghetti}} \frac{1}{[3.5\ln(R/r_c)]^{1/2}}. \quad (25)$$

Varying R between scales of 1 m to 10^{-12} m varies the logarithmic factor between around 2 to 7, and

$$\frac{(L/d)_{\mathrm{spaghetti}}}{(L/d)_{\mathrm{lasagna}}} \approx 7\text{--}25, \quad (26)$$

i.e., the order of the spaghettitype phases will be an order of magnitude larger than the order of the lasagnatype phases.

The configurations corresponding to the local minima in Fig. 6 have $W_{C+L} = 13\text{--}19$ keV, $(r_c - r_N)/r_c = 0.21$ for spaghetti, and 0.5 for lasagna (taking the RMS radius of the cluster in our simulations). Assuming no collectivity, $A_{\mathrm{cell}}/A_{\mathrm{collective}} = 614$ and

$$(L/d)_{\mathrm{spaghetti}} \approx 40. \quad (27)$$

Assuming complete collectivity, $A_{\mathrm{cell}}/A_{\mathrm{collective}} = 1$,

$$(L/d)_{\mathrm{spaghetti}} \lesssim 2, \quad (28)$$

and matter is completely disordered.

From this, the domains containing the spaghetti phase have a length scale of 40 lattice spacings, and the two waffle phases which are similar to lasagna phases (with holes in), are ordered on the length scale $L/d_{\mathrm{lasagna}} \sim$ two lattice spacings (and are therefore very disordered) at the fictive temperature.

The more nucleons behave collectively, the temperature at which matter becomes frozen into local minima will increase, and the scale on which the matter is ordered decreases. Therefore, our estimates above give *upper* limits on the distance scales over which pasta is ordered.

We can also conclude that fluctuations in the average density and electron fraction, of order 5–10% occur on microscopic scales of no more than around 10 lattice spacings at this depth.

In the next section, we now go through the crust from the lowest to highest densities we performed calculations at, spanning the pasta phases. We will present the Gibbs free-energy surfaces calculated in the same way as presented in this section, the resulting equilibrium fractions of the different phases, and the upper limit to the length scale of their domains derived from the fictive temperature.

B. The onset of pasta: $n_b \approx 0.035$ fm^{-3}–0.045 fm^{-3}

In Figs. 7–9, we show the Gibbs free-energy surfaces at proton fractions of $y_p = 0.018$, 0.022, and 0.026 in a cell with 454 nucleons in total for calculations performed around
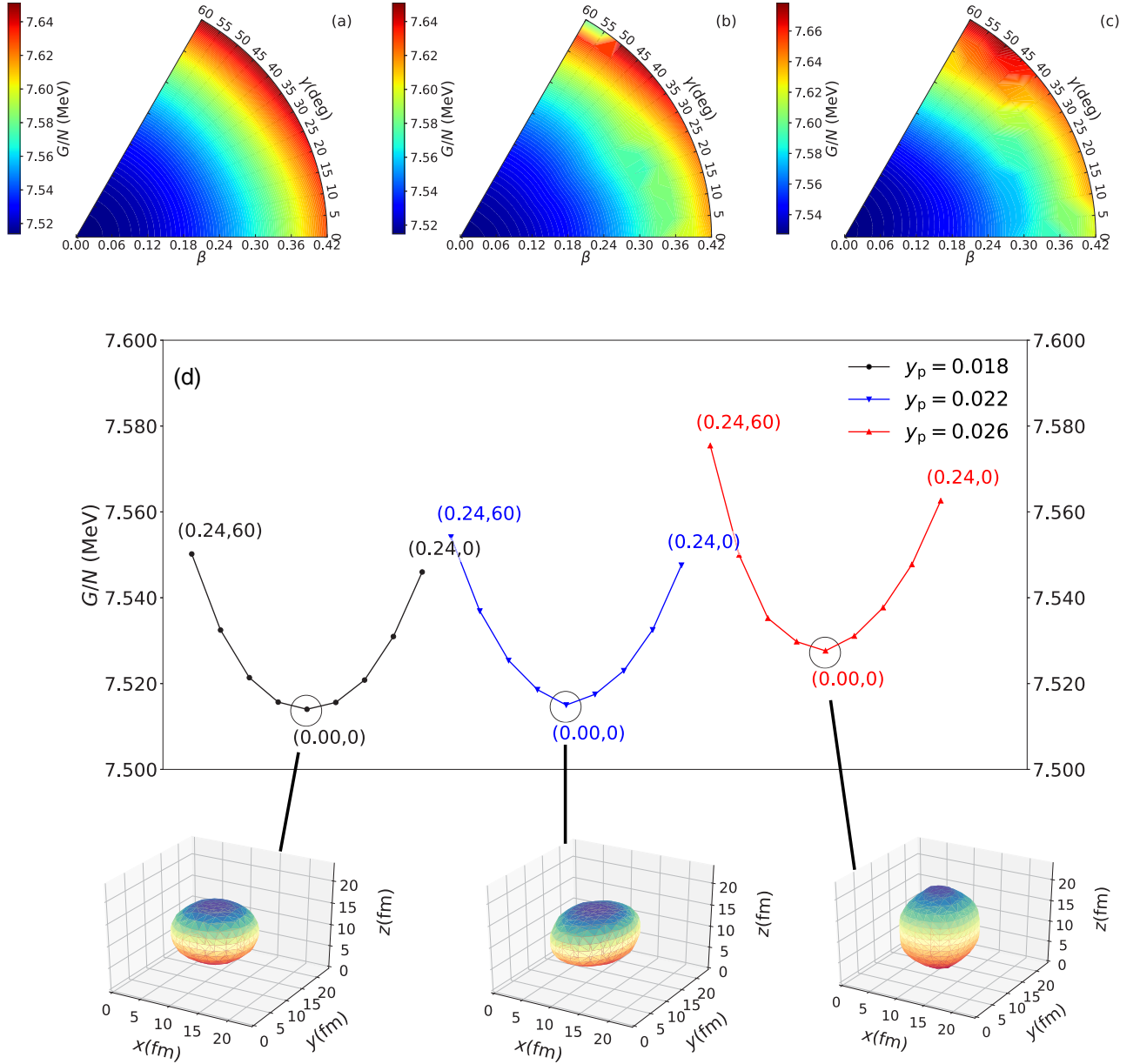
FIG. 7. Top row: Gibbs free-energy surfaces at a pressure of 0.094 MeV fm^{-3} corresponding to a baryon density of $\approx$0.035 fm^{-3} at proton fractions of 0.018 (a), 0.022 (b), and 0.026 (c), for cells containing $A_{\mathrm{cell}} = 454$ nucleons. Below is the Gibbs free-energy variation along one dimensional paths passing through the energy minimum (d). Selected (β, γ) coordinates are shown along the one-dimensional plots. Visualizations of the minimum energy nuclear shapes are shown, obtained by plotting a surface of constant neutron density corresponding to the average neutron density in the cell. In all cases the minimum is a spherical nucleus.

$n_{\mathrm{b}} = 0.035$ fm^{-3}, $n_{\mathrm{b}} = 0.04$ fm^{-3}, and $n_{\mathrm{b}} = 0.045$ fm^{-3}, respectively. The Gibbs energy surfaces are calculated at constant pressures of $P = 0.094$, 0.12, and 0.15 MeV fm^{-3}, respectively (corresponding to the pressure of the spherical configuration at $y_{\mathrm{p}} = 0.022$ and a density of $n_{\mathrm{b}} = 0.035$ fm^{-3}, $n_{\mathrm{b}} = 0.04$ fm^{-3}, and $n_{\mathrm{b}} = 0.045$ fm^{-3}).

At $P = 0.094$ MeV fm^{-3}, $n_{\mathrm{b}} \approx 0.035$ fm^{-3}, there is a single global minimum at each proton fraction at $(\beta, \gamma) = (0, 0°)$ corresponding to a spherical nucleus. No other local minima are present. We have not yet entered the pasta phases.

At both $P = 0.12$ MeV fm^{-3}, $n_{\mathrm{b}} \approx 0.04$ fm^{-3} and $P = 0.15$ MeV fm^{-3}, $n_{\mathrm{b}} \approx 0.045$ fm^{-3}, more structure starts to appear in the energy surface. Some of these structures are local minima corresponding to the first appearance of the nuclear pasta configuration. The variation in Gibbs free energy along trajectories in the energy surface at $P = 0.12$ MeV fm^{-3} and 0.15 MeV fm^{-3} are shown in Figs. 8 and 9.

At $P = 0.12$ MeV fm^{-3} the fictive temperature is $kT_{\mathrm{f}} = 73$ keV $\rightarrow T_8 = 8.5$ (where $T_8 = T/10^8$K), and we see the minimum is still a spherical nuclear phase. A local minima 41 keV above the global minimum corresponding to
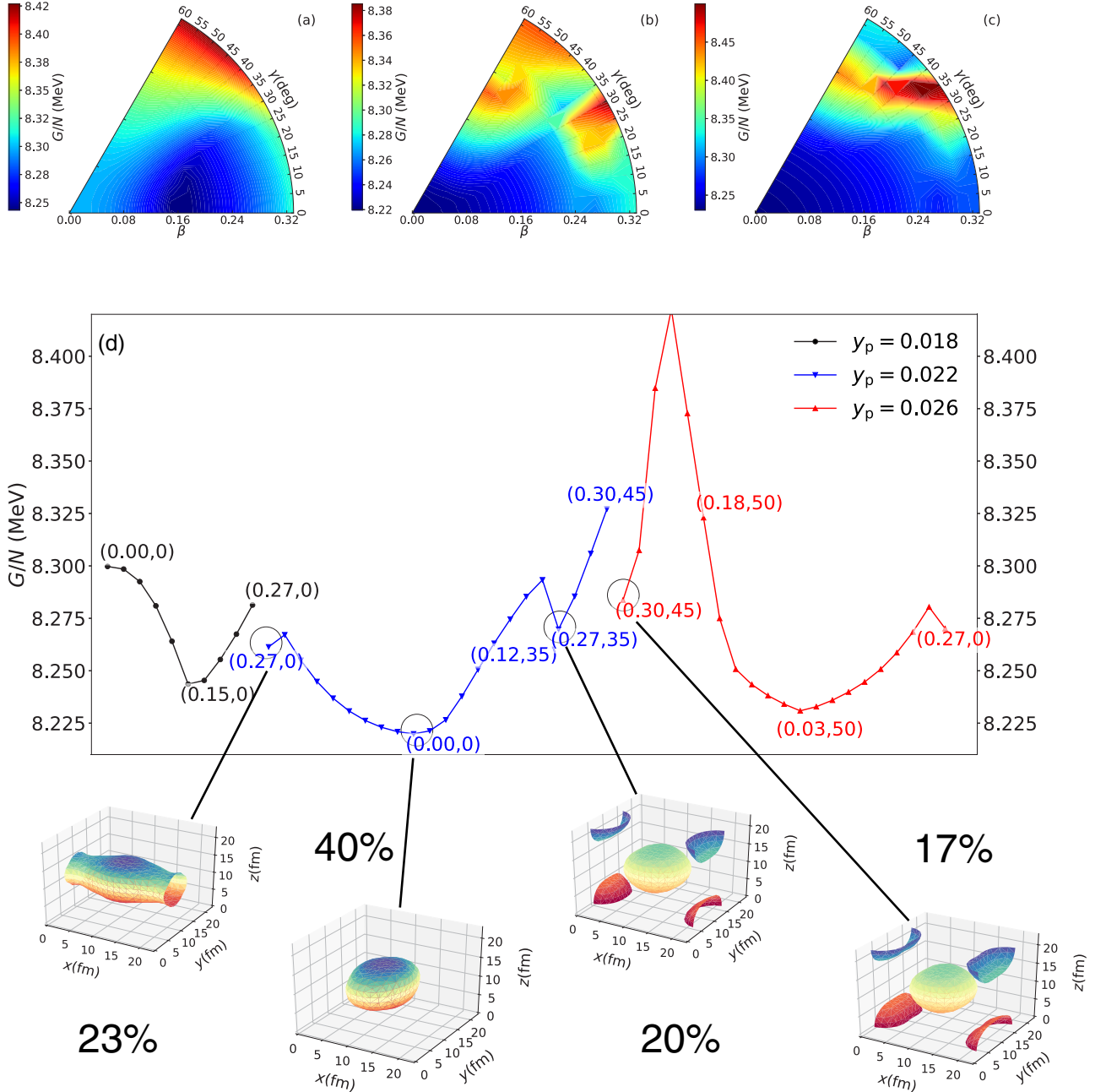
FIG. 8. Top row: Gibbs free-energy surfaces at a pressure of $0.120\,\mathrm{MeV\,fm^{-3}}$, corresponding to a baryon density of $\approx 0.04\,\mathrm{fm^{-3}}$, at proton fractions of 0.018 (a), 0.022 (b), and 0.026 (c), for cells containing $A_{\mathrm{cell}} = 454$ nucleons. Below is the Gibbs free-energy variation along one dimensional paths passing through the energy minimum (d). Selected (β, γ) coordinates are shown along the one-dimensional plots. Visualizations of the minimum energy nuclear shapes are shown, obtained by plotting a surface of constant neutron density corresponding to the average neutron density in the cell. The minimum energy nuclear shape is roughly spherical, but deformed nuclear and cylindrical nuclear shapes appear as local minima. The relative abundances of the phases at a temperature equal to the fictive temperature is shown next to the visualizations of the phases.

a spaghetti phase appears at $y_{\mathrm{p}} = 0.022$. Two local minima corresponding to elongated isolated nuclei in a 2D lattice, analogous to the smectic-B phases of liquid crystals, appear at $y_{\mathrm{p}} = 0.022$ and $y_{\mathrm{p}} = 0.026$, at heights 50 and 64 keV above the global minimum. Using these numbers, the relative abundances of the spherical:spaghetti:deformed nucleus($y_{\mathrm{p}} = 0.022$): deformed nucleus($y_{\mathrm{p}} = 0.026$) phases are 0.40:0.23:0.20:0.17.

At $P = 0.15\,\mathrm{MeV\,fm^{-3}}$ the fictive temperature is $kT_{\mathrm{f}} = 34$ keV $\rightarrow T_8 = 4.0$, we see the same three phases, with the elongated nuclear phase appearing 21 keV and the spaghetti phase 25 keV above the global minimum of spherical nuclei. Note the fictive temperature and energy separation of minima is decreasing with density. The ratios of spherical nuclei:elongated nuclei:spaghetti are 0.50:0.27:0.24.
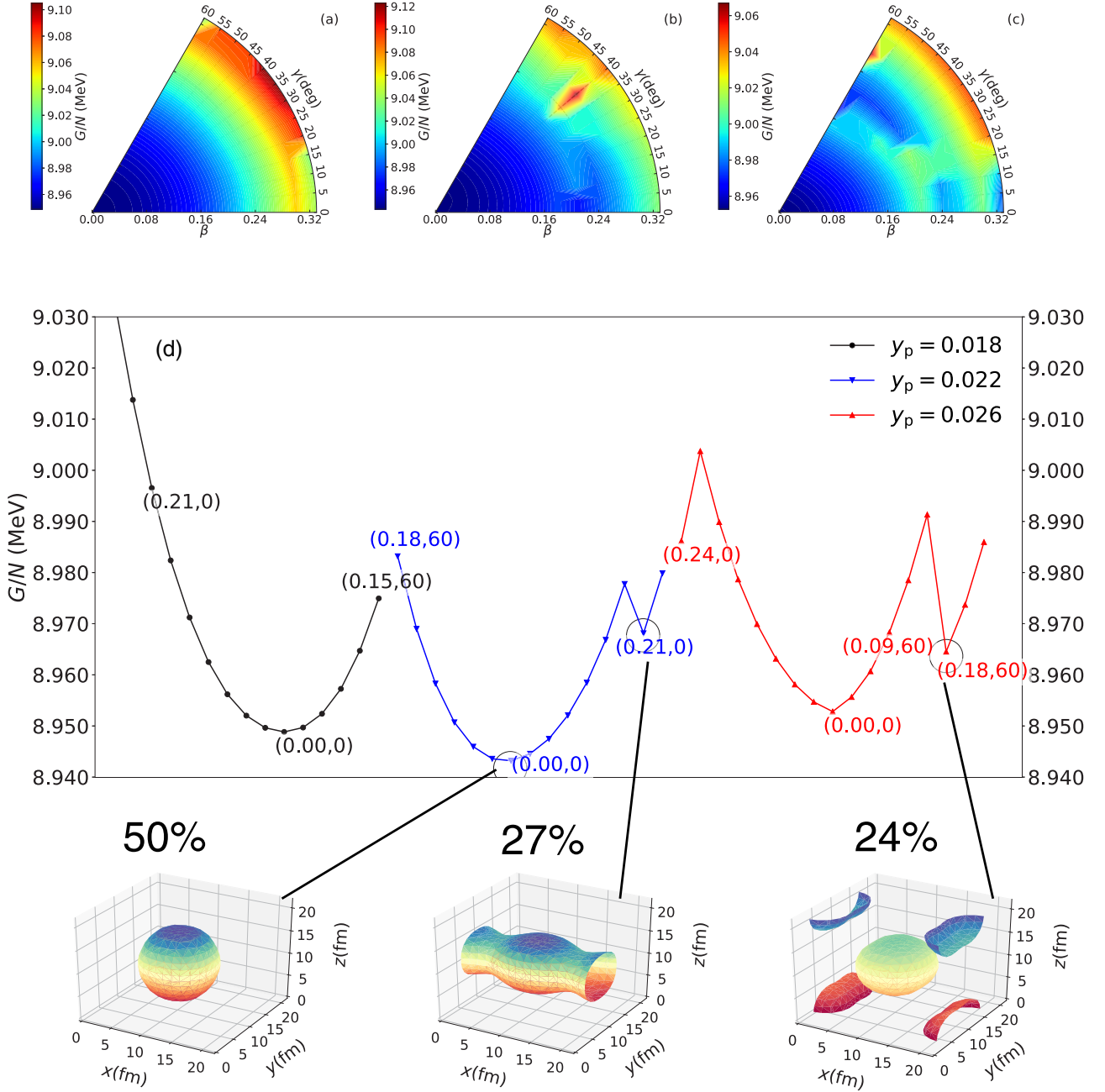
FIG. 9. Top row: Gibbs free-energy surfaces at a pressure of $0.150\,\mathrm{MeV\,fm^{-3}}$, corresponding to a baryon density of $\approx 0.045\,\mathrm{fm^{-3}}$, at proton fractions of 0.018 (a), 0.022 (b), and 0.026 (c), for cells containing $A_{\mathrm{cell}} = 454$ nucleons. Below is the Gibbs free-energy variation along one dimensional paths passing through the energy minimum (d). Selected (β, γ) coordinates are shown along the one-dimensional plots. Visualizations of the minimum energy nuclear shapes are shown, obtained by plotting a surface of constant neutron density corresponding to the average neutron density in the cell. The minimum energy nuclear shape is roughly spherical, but deformed nuclear and cylindrical nuclear shapes appear as local minima. The relative abundances of the phases at a temperature equal to the fictive temperature is shown below the visualizations of the phases.

In Fig. 10 we show a representative set of baryon density surfaces, for calculations performed around $n_{\mathrm{b}} = 0.045\,\mathrm{fm^{-3}}$. The fluctuations in baryon density between local minima are small at these depths, of order 1% of the average density.

The lattice energy of the spaghetti phases from the quantum calculations is 18 keV per nucleon and 13 keV per nucleon for pressures of $P = 0.12\,\mathrm{MeV\,fm^{-3}}$ and $0.15\,\mathrm{MeV\,fm^{-3}}$, respectively, and the corresponding length

scale of the spaghetti domains is ≈ 7 times the lattice spacing in both cases ($\approx 150\,\mathrm{fm}$). In the case of $P = 0.12\,\mathrm{MeV\,fm^{-3}}$ 10% of the composition is at a proton fraction of 0.026, so fluctuations in average proton fraction occur of order 20% on length scales of $\sim 150\,\mathrm{fm}$.

This region in which pasta first appears as local minima above a ground state is the first of four distinct pasta regimes we will encounter, and ranges from $n_{\mathrm{b}} \approx 0.04\,\mathrm{fm^{-3}}$ up to
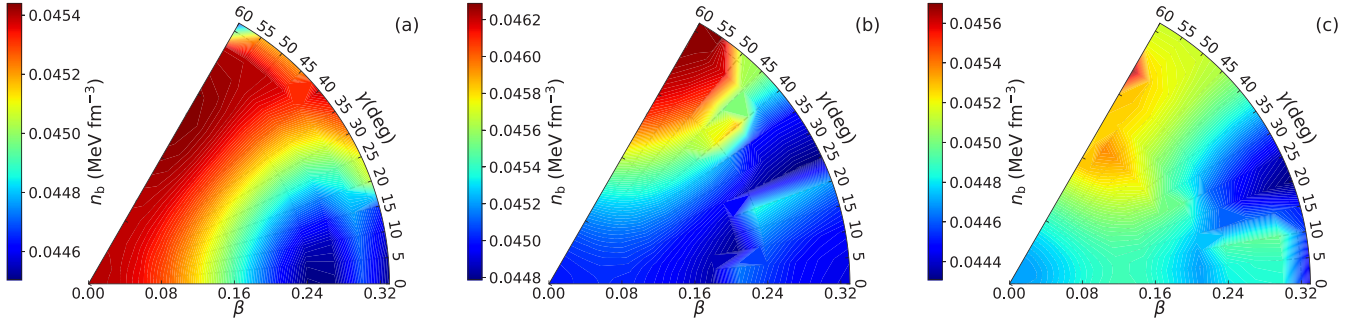
FIG. 10. Average baryon density surfaces (bottom) at a constant pressure of $0.15\,\text{MeV}\,\text{fm}^{-3}$, corresponding to a baryon density of $\approx 0.045\,\text{fm}^{-3}$, for cells containing $A_{\text{cell}} = 454$ nucleons. Results are shown for proton fraction of 0.018 (a), 0.022 (b), and 0.026 (c). The local minima differ in baron density by of order 5%.

$n_{\text{b}} \approx 0.05\,\text{fm}^{-3}$. It is characterized by spherical nuclei being the absolute ground state, but spaghetti phases and highly deformed nuclei appearing as closely separated local minima, accounting for about over half of the material in the crust at the fictive temperature. Spaghetti phases constitute $\approx 25\%$ of the material at these densities at the fictive temperatures of 4–$8 \times 10^8\,\text{K}$. If annealing takes place over sufficiently long timescales, then in this regime all matter will eventually be converted to spherical nuclei.

C. Pasta is established, but spherical nuclei still exist: $n_{\text{b}} \approx 0.05\,\text{fm}^{-3}$ and $0.054\,\text{fm}^{-3}$

In Fig. 11 we show the Gibbs free-energy surfaces at proton fractions of $y_{\text{p}} = 0.021$, 0.023, and 0.025 at a constant pressure $P = 0.184\,\text{MeV}\,\text{fm}^{-3}$ (densities around $n_{\text{b}} = 0.05\,\text{fm}^{-3}$) in a cell containing 956 nucleons. In Fig. 12 we show the Gibbs free-energy surfaces at proton fractions of $y_{\text{p}} = 0.022$, 0.024, and 0.026 at a constant pressure $P = 0.234\,\text{MeV}\,\text{fm}^{-3}$ (densities around $n_{\text{b}} = 0.054\,\text{fm}^{-3}$) in a cell containing 1166 nucleons. In both cases, one can see that the energy surfaces are becoming much richer in structure, with numerous local minima. In each case we identify three minima accessible to all others by continuous deformation and adjustment of proton fraction without increasing energy.

We see that at both densities isolated nuclei are still present, but they are no longer always the absolute minimum. At $P = 0.184\,\text{MeV}\,\text{fm}^{-3}$ the absolute minimum is the nuclear 'waffle' phase, with a corrugated spaghetti phase also appearing as a local minimum. The minima occur at two different proton fractions, pointing to possible fluctuations in average proton fraction of order 10%. At $P = 0.234\,\text{MeV}\,\text{fm}^{-3}$ the isolated nuclear phase is—just—the absolute minimum, almost equal in energy to the spaghetti phase. Again, a waffle phase appears as a local minimum.

At $P = 0.184\,\text{MeV}\,\text{fm}^{-3}$ the fictive temperature kT_{f} is $21\,\text{keV} \rightarrow T_8 = 2.4$, and $\Delta G_{21} = 14\,\text{keV}$ and $\Delta G_{31} = 26\,\text{keV}$. The relative abundances at T_{f} are waffle:spherical:spaghetti are 0.55:0.29:0.16.

At $P = 0.234\,\text{MeV}\,\text{fm}^{-3}$ the fictive temperature kT_{f} is $11\,\text{keV} \rightarrow T_8 = 1.3$ and $\Delta G_{21} = 4\,\text{keV}$ and $\Delta G_{31} = 6\,\text{keV}$. The ratios of minima 1(spherical):2(spaghetti):3(waffle) are 0.44:0.31:0.25.

The lattice energy of the spaghetti and waffle phases from the quantum calculations are 23 keV per nucleon and 17 keV per nucleon, respectively, for $P = 0.184\,\text{MeV}\,\text{fm}^{-3}$ and 24 keV per nucleon and 20 keV per nucleon, respectively, for $P = 0.234\,\text{MeV}\,\text{fm}^{-3}$.

Waffles are really a form of lasagna with a density modulation along its surface, and we can estimate its long-range order as that of lasagna. It is of order two to three lattice spacings for $P = 0.184\,\text{MeV}\,\text{fm}^{-3}$ and $P = 0.234\,\text{MeV}\,\text{fm}^{-3}$—indicating these phases are almost completely disordered. The corresponding length scale of the spaghetti domains from is 19 and 25 times the lattice spacing (500–600 fm) for $P = 0.184\,\text{MeV}\,\text{fm}^{-3}$ and $P = 0.234\,\text{MeV}\,\text{fm}^{-3}$, respectively. Fluctuations of proton fraction of order 10% occur on these length scales.

In this regime of pasta, the pasta shapes have for the most part become the ground state, but spherical nuclei still appear as local minima (and can occasionally appear as the global minimum). If annealing takes place, on sufficiently long timescales, then all matter in this regime will be converted to pasta. The fictive temperature has dropped to a 1–$3 \times 10^8\,\text{K}$. At each density in this regime, isolated nuclei, spaghetti and waffles coexist at the fictive temperature.

D. Exclusively pasta but protons are still localized to the pasta structures

In the density region between around $0.055\,\text{fm}^{-3}$ to $0.065\,\text{fm}^{-3}$, isolated nuclei cease to be local minima at all, so we have entered the regime of pure pasta. We have already detailed a representative set of configurations at $0.06\,\text{fm}^{-3}$. Waffles and spaghetti are the coexisting phases in this density window. Protons are still localized in at least one dimension.

E. Protons are delocalized

In Figs. 13–15, we show the Gibbs free-energy surfaces at pressures of $P = 0.30\,\text{MeV}\,\text{fm}^{-3}$, $0.32\,\text{MeV}\,\text{fm}^{-3}$, and $0.34\,\text{MeV}\,\text{fm}^{-3}$ corresponding to densities around $n_{\text{b}} = 0.066\,\text{fm}^{-3}$, $0.07\,\text{fm}^{-3}$, and $n_{\text{b}} = 0.076\,\text{fm}^{-3}$. The cells contain 784, 532, and 532 nucleons, respectively.
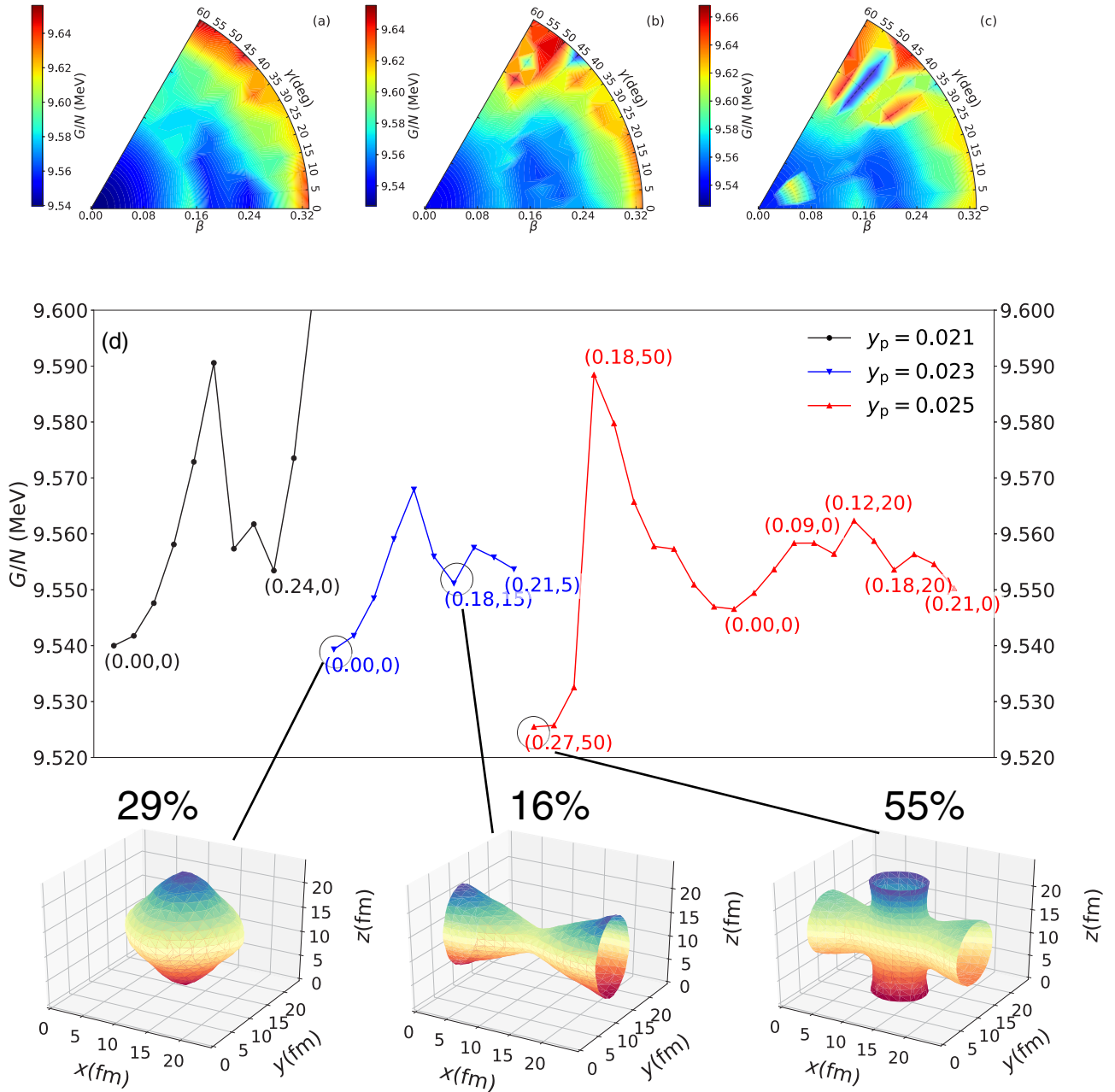
FIG. 11. Top row: Gibbs free-energy surfaces at a pressure of $0.184 \, \text{MeV fm}^{-3}$, corresponding to a baryon density of $\approx 0.05 \, \text{fm}^{-3}$, at proton fractions of 0.021 (a), 0.023 (b), and 0.025 (c), for cells containing $A_{\text{cell}} = 956$ nucleons. Below is the Gibbs free-energy variation along one-dimensional paths passing through the energy minimum (d). Selected (β, γ) coordinates are shown along the one-dimensional plots. Visualizations of the minimum energy nuclear shapes are shown, obtained by plotting a surface of constant neutron density corresponding to the average neutron density in the cell. The minimum energy nuclear shape is a nuclear "waffle," with an isolated nuclear phase and spaghetti phase as local minima at a different proton fraction. The relative abundances of the phases at a temperature equal to the fictive temperature is shown below the visualizations of the phases.

At $P = 0.30 \, \text{MeV fm}^{-3}$, $n_{\text{b}} = 0.066 \, \text{fm}^{-3}$, we perform calculations at proton fractions of $y_{\text{p}} = 0.022$, 0.025, and 0.028. The minimum energy configuration is the bicontinuous cubic-P (BCP) phase—essentially a nucleus joined in all three directions to adjacent nuclei, allowing the protons to be entirely delocalized. Both cluster and external neutron fluid form two interlaced, continuous domains through space. Lasagna and spaghetti phases make up the two remaining unique local minima. At $P = 0.32 \, \text{MeV fm}^{-3}$ and $P = 0.34 \, \text{MeV fm}^{-3}$, $(n_{\text{b}} = 0.07 \, \text{fm}^{-3}$ and $n_{\text{b}} = 0.076 \, \text{fm}^{-3})$ we perform calculations at proton fractions of $y_{\text{p}} = 0.030$, 0.034, 0.038, and 0.42. At the lower of those two densities, the absolute minimum corresponds to the lasagna phase, with waffle and BCP phases making up the remaining unique local minima. At the higher
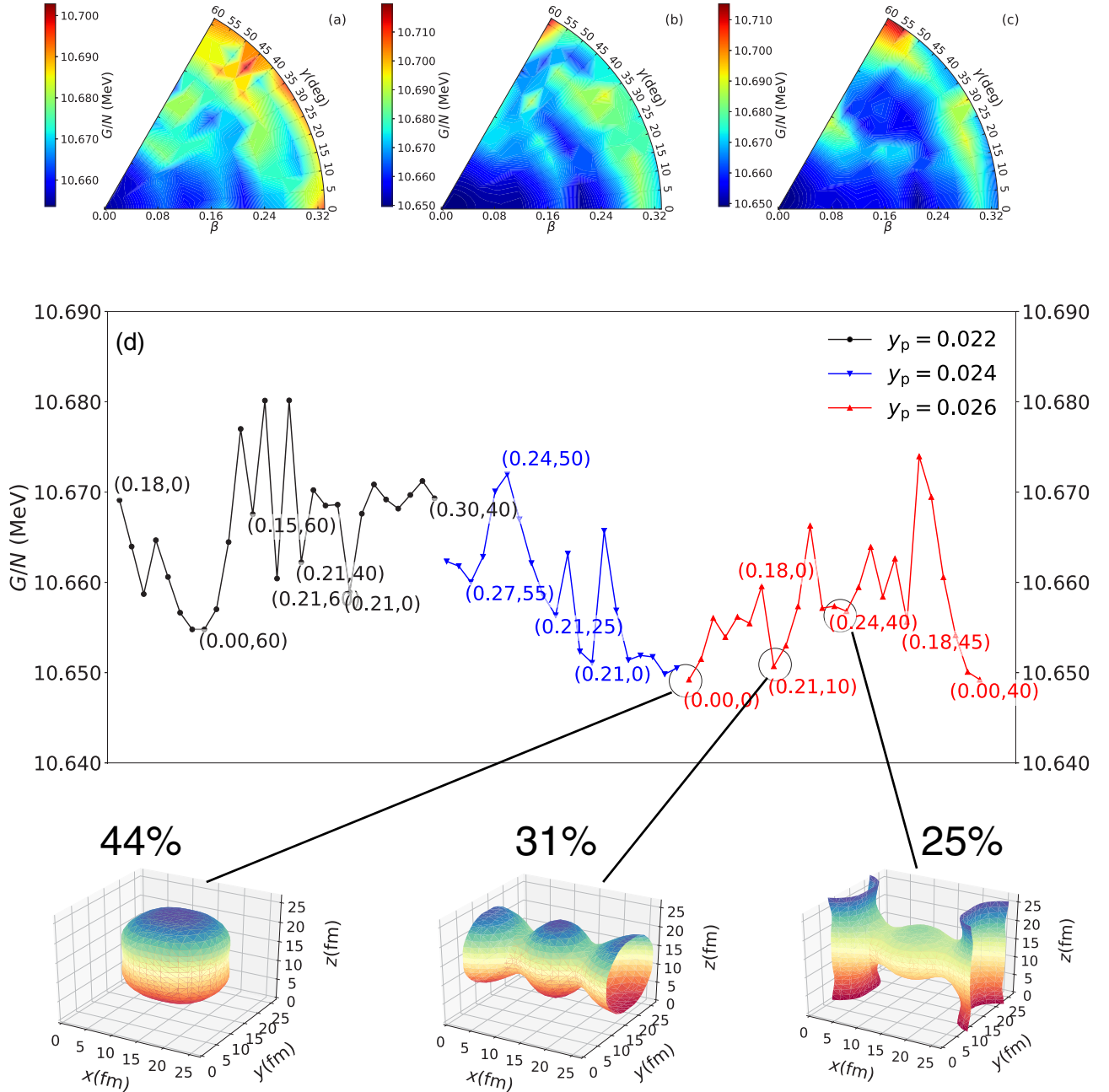
FIG. 12. Top row: Gibbs free-energy surfaces at a pressure of 0.234 MeV fm^{-3}, corresponding to a baryon density of $\approx$0.054 fm^{-3}, at proton fractions of 0.022 (a), 0.024 (b), and 0.026 (c), for cells containing $A_{cell} = 1166$ nucleons. Below is the Gibbs free-energy variation along one dimensional paths passing through the energy minimum (d). Selected (β, γ) coordinates are shown along the one-dimensional plots. Visualizations of the minimum energy nuclear shapes are shown, obtained by plotting a surface of constant neutron density corresponding to the average neutron density in the cell. The minimum energy nuclear shape is roughly spherical, followed by cylindrical and waffle shapes. The relative abundances of the phases at a temperature equal to the fictive temperature is shown below the visualizations of the phases.

density, all minima correspond to variations of the BCP phases at two different proton fractions $y_p = 0.034, 0.038$. Therefore, the three main phases that coexist in this range of densities are spaghetti, waffles, lasagna, and the BCP phase.

At $P = 0.30$ MeV fm^{-3}, $n_b = 0.066$ fm^{-3}, the fictive temperature kT_f is 7.4 keV $\rightarrow T_8 = 0.85$, and $\Delta G_{21} = 1$ keV and $\Delta G_{31} = 5$ keV. The ratios of BCP:lasagna:spaghetti are 0.42:0.37:0.21. The lattice energy of the lasagna phase from

the quantum calculations is 7 keV per nucleon and for the spaghetti phase it is 11 keV per nucleon. For the spaghetti phases, our estimated domain sizes at the fictive temperature is 22 lattice spacings, and for the lasagna is about three lattice spacings.

At $P = 0.32$ MeV fm^{-3}, $n_b = 0.07$ fm^{-3}, the fictive temperature kT_f is 14 keV $\rightarrow T_8 = 1.7$, and $\Delta G_{21} = 10$ keV and $\Delta G_{31} = 10$ keV. The ratios of lasagna:waffle:BCP are
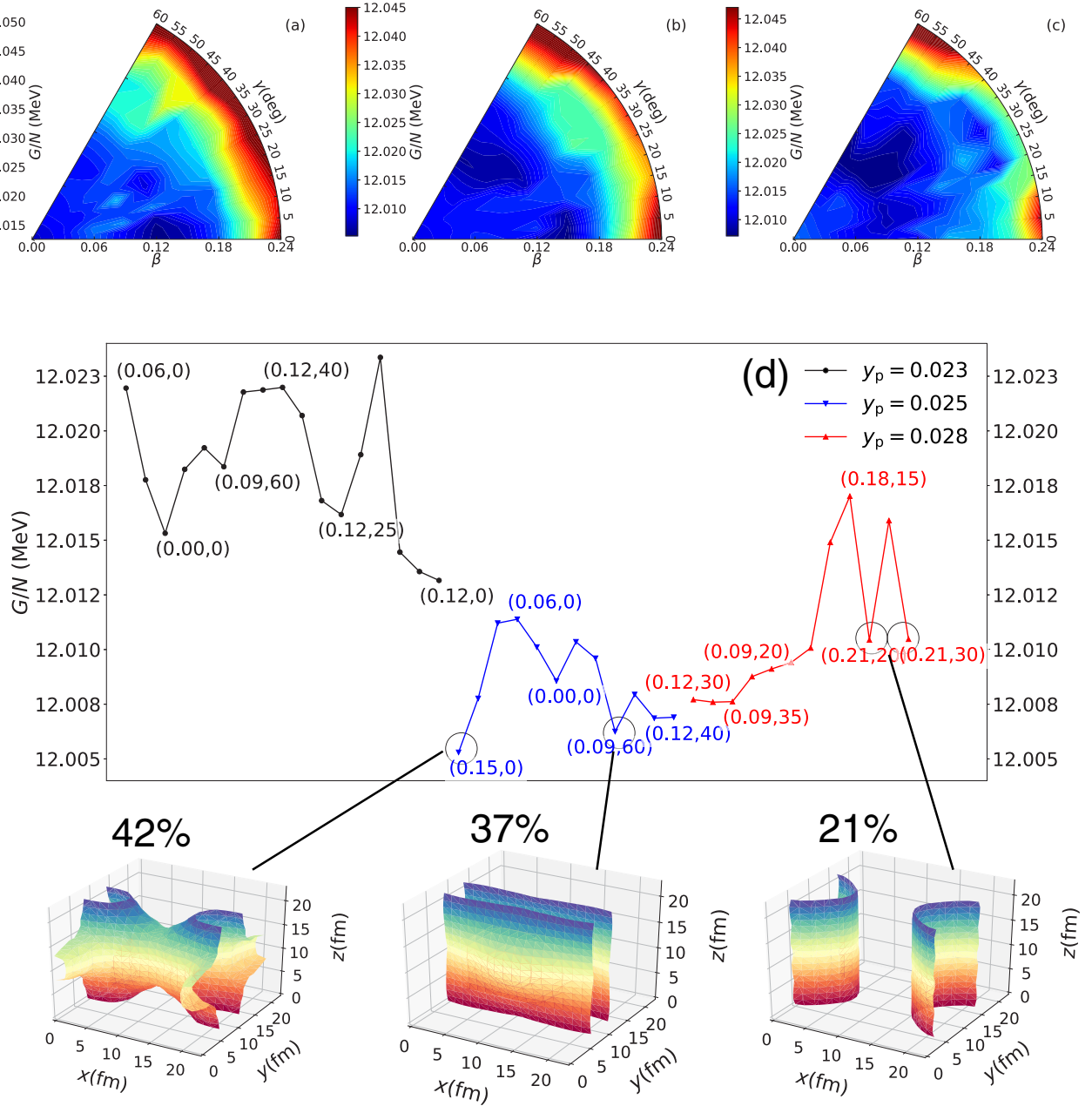
FIG. 13. Top row: Gibbs free-energy surfaces at a pressure of 0.30 MeV fm^{-3}, corresponding to a baryon density of ≈ 0.066 fm^{-3}, at proton fractions of 0.022 (a), 0.025 (b), and 0.028 (c), for cells containing $A_{cell} = 784$ nucleons. Below is the Gibbs free-energy variation along one dimensional paths passing through the energy minimum (d). Selected (β, γ) coordinates are shown along the one-dimensional plots. Visualizations of the minimum energy nuclear shapes are shown, obtained by plotting a surface of constant neutron density corresponding to the average neutron density in the cell. The minimum energy nuclear configuration is the bicontinuous cubic-P phase, followed by planar and cylindrical geometries. The relative abundances of the phases at a temperature equal to the fictive temperature is shown below the visualizations of the phases.

0.49:0.26:0.25. The lattice energy of both lasagna and waffle phases is 6 keV per nucleon, and their estimated domain size is approximately one lattice spacing.

At $P = 0.34$ MeV fm^{-3}, $n_b = 0.076$ fm^{-3} the fictive temperature kT_f is 16 keV $\rightarrow T_8 = 2.0$, and $\Delta G_{21} = 0.3$ keV and $\Delta G_{31} = 3$ keV. The ratios of the abundances of all three BCP phases are 0.36:0.35:0.29. The BCP phase is stabilized with respect to thermodynamic fluctuations of the type explored in this paper, so in this density region it is possible that the order of matter is much longer than density regions where the BCP phase is not the only nuclear geometry.

In Fig. 16 we show the baryon density surfaces at a pressure of $P = 0.34$ MeV fm^{-3}. Variations from local minimum to local minimum are around 5% that of the average baryon density.

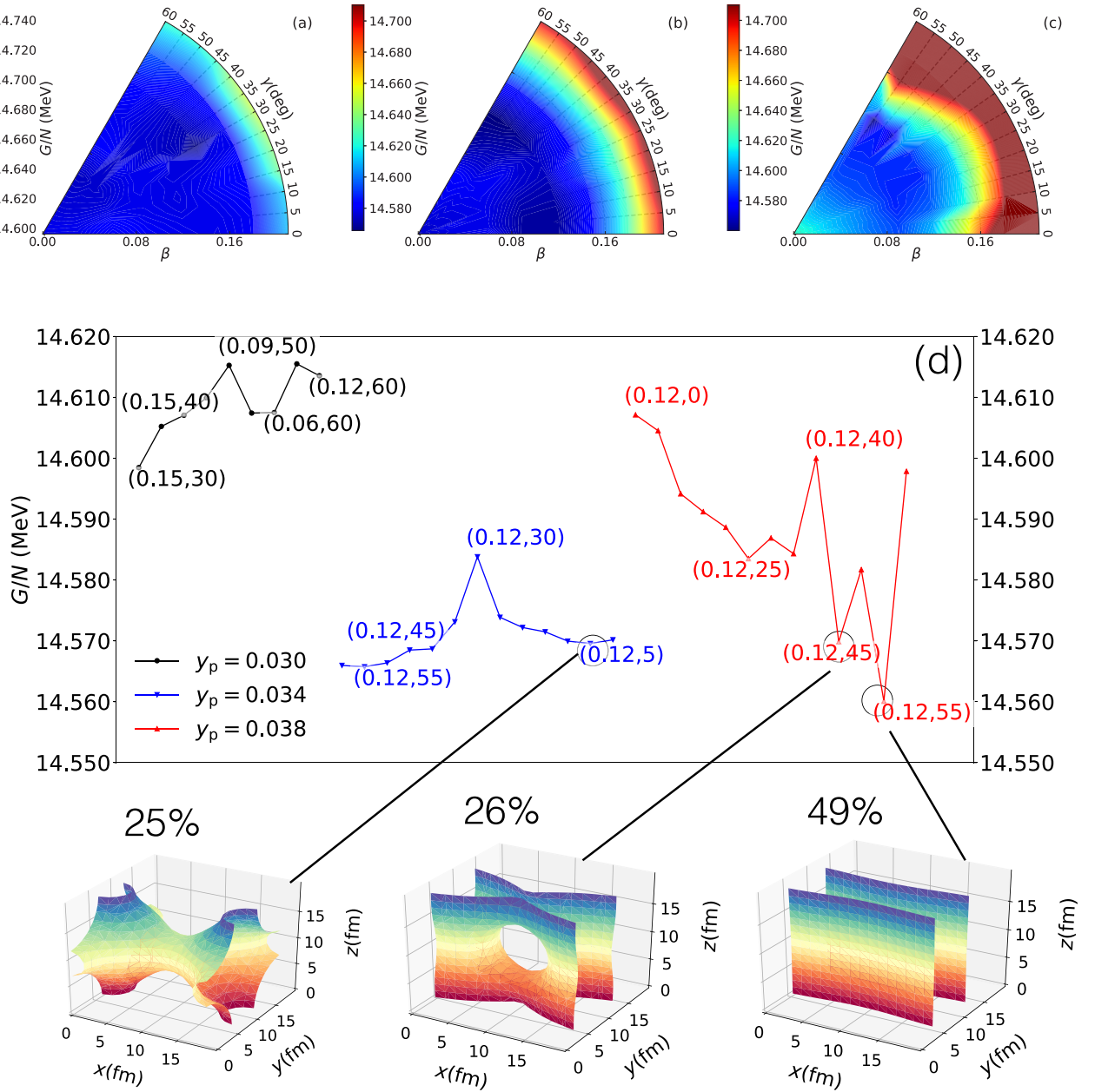FIG. 14. Top row: Gibbs free-energy surfaces at a pressure of 0.32 MeV fm^{-3}, corresponding to a baryon density of ≈ 0.07 fm^{-3}, at proton fractions of 0.03 (a), 0.034 (b), and 0.038 (c), for cells containing $A_{\text{cell}} = 532$ nucleons. Below is the Gibbs free-energy variation along one dimensional paths passing through the energy minimum. Selected (β, γ) coordinates are shown along the one-dimensional plots. Visualizations of the minimum energy nuclear shapes are shown, obtained by plotting a surface of constant neutron density corresponding to the average neutron density in the cell. The minimum energy nuclear configuration is planar, followed by waffle and bicontinuous cubic-P phases. The relative abundances of the phases at a temperature equal to the fictive temperature is shown below the visualizations of the phases.

Moving up in density, in Figs. 17 and 18, we show the Gibbs free-energy surfaces at pressures of $P = 0.45$ MeV fm^{-3} and 0.53 MeV fm^{-3} corresponding to densities around $n_b = 0.082$ fm^{-3} and 0.088 fm^{-3}. In each case the cells contain 332 nucleons, and we calculate energy surfaces at proton fractions of $y_p = 0.24$, 0.3, and 0.36. We see that as we get close to the crust-core transition, the energy surfaces are becoming simpler in their structure. In both cases, two minima appear.

At $P = 0.45$ MeV fm^{-3}, the two minima are at a proton fraction of 0.03. The higher-lying one is a spaghettilike configuration; the absolute minimum is a more complex configuration, consisting of cylindrical holes (antispaghetti) and spaghetti. To reveal the structure requires plotting the two isosurfaces at low and high density, as shown in Fig. 17; the low density isosurface (about half the average neutron density) is shown on the left and reveals the cylindrical hole; on the right, at high density (about three-quarters the
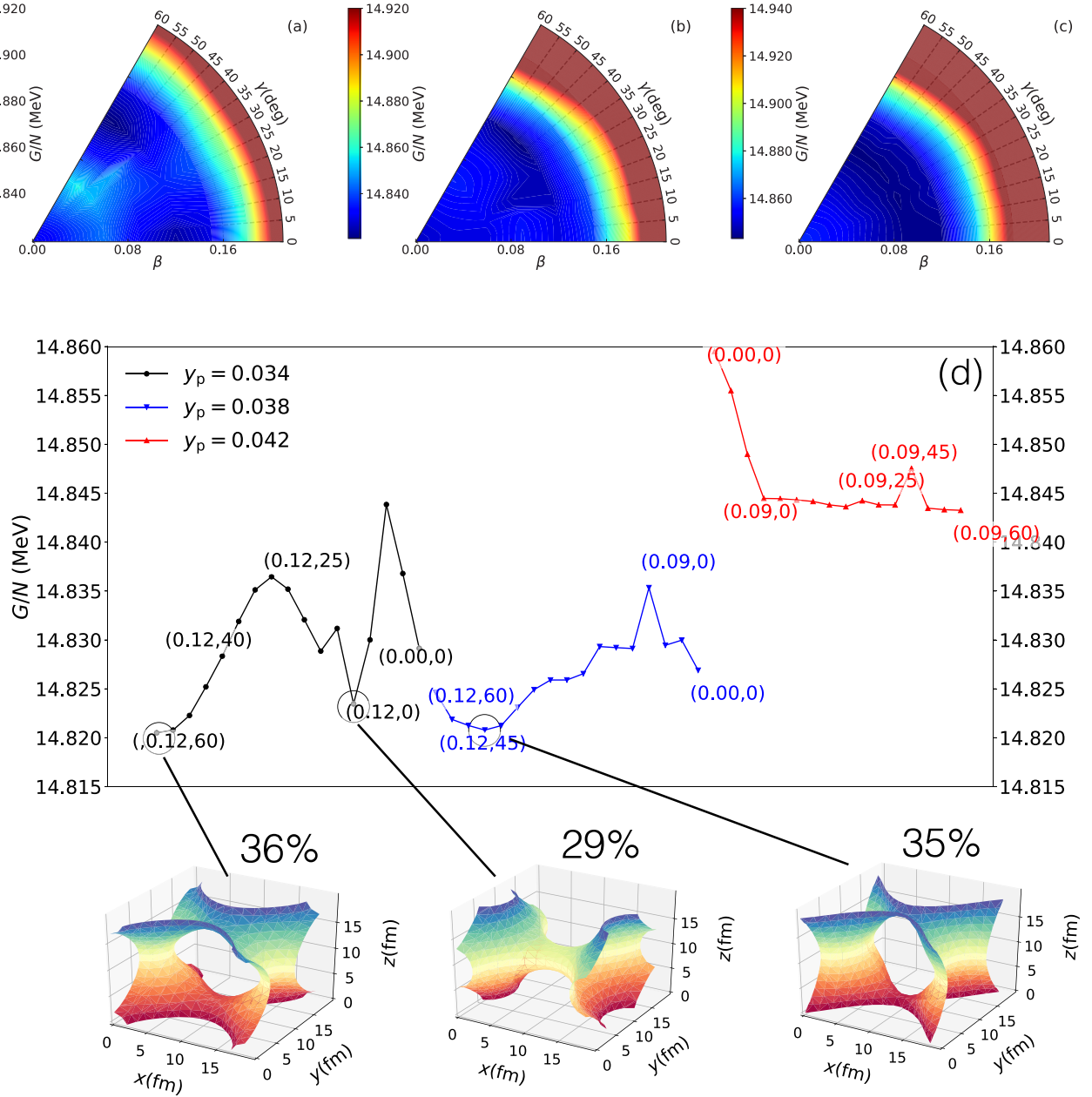
FIG. 15. Top row: Gibbs free-energy surfaces at a pressure of 0.34 MeV fm^{-3}, corresponding to a baryon density of ≈ 0.076 fm^{-3}, at proton fractions of 0.034 (a), 0.038 (b), and 0.042 (c), for cells containing $A_{\text{cell}} = 532$ nucleons. Below is the Gibbs free-energy variation along one dimensional paths passing through the energy minimum (d). Selected (β, γ) coordinates are shown along the one-dimensional plots. Visualizations of the minimum energy nuclear shapes are shown, obtained by plotting a surface of constant neutron density corresponding to the average neutron density in the cell. All three minima are variations of the bicontinuous cubic-P phase, albeit at different proton fractions. The relative abundances of the phases at a temperature equal to the fictive temperature is shown below the visualizations of the phases.

average neutron density in the cell) the spaghetti structure is revealed. In the bulk, protons as well as neutrons are delocalized.

At $P = 0.53$ MeV fm^{-3}, the absolute minimum is at a proton fraction of 0.036 and corresponds to a lasagna structure. A local minimum appears at a proton fraction of 0.3 and corresponds to the same spaghetti-antispaghetti configuration seen at the previous density.

At $P = 0.45$ MeV fm^{-3}, the fictive temperature kT_{f} is 16 keV $\rightarrow T_8 = 1.9$, and $\Delta G_{21} = 3.5$ keV. The ratios of spaghetti hole:spaghetti are 0.55:0.45. The lattice energy of the spaghetti phase is 3.7 keV per nucleon, and their estimated domain size is approximately four lattice spacings. The lattice energy of the spaghetti hole is 2.9 keV per nucleon, with a domain size similar order.

At $P = 53$ MeV fm^{-3}, the fictive temperature kT_{f} is 4.6 keV $\rightarrow T_8 = 0.53$, and $\Delta G_{21} = 2$ keV. The ratios of
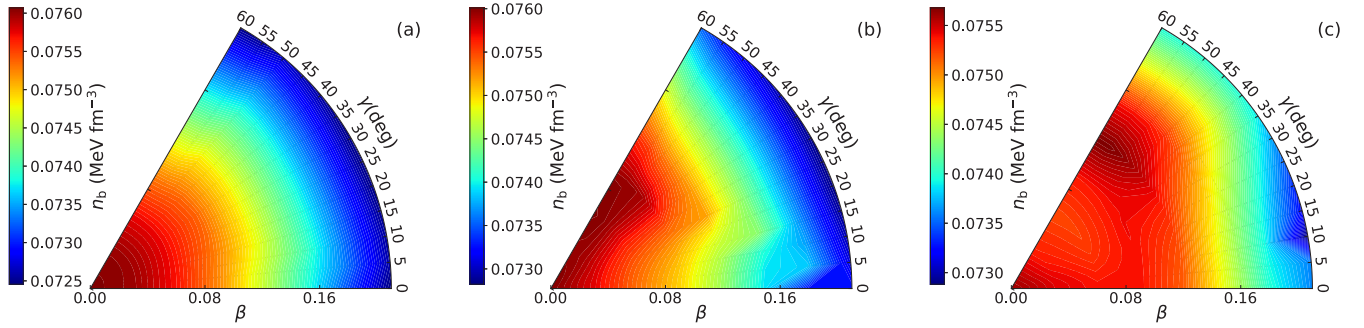
FIG. 16. Average baryon density surfaces (bottom) at a constant pressure of 0.524 MeV fm^{-3}, corresponding to a baryon density of $\approx$0.076 fm^{-3}, for cells containing $A_{cell} = 532$ nucleons. Results are shown for proton fraction of 0.034 (a), 0.038 (b), and 0.042 (c). The local minima differ in baron density by of order 5%.

lasagna:spaghetti hole are 0.6:0.4. The lattice energy of the lasagna phase is 1.8 keV per nucleon, and the lattice energy of the spaghetti hole is 1.6 keV per nucleon. The estimated domain size is approximately two lattice spacings for the lasagna and significantly less than 1 lattice spacing for the spaghetti hole.

The spaghetti phases, the first pasta to appear as one descends through the crust, can persist to relatively deep layers, making them the most robust of the pasta phases.

IV. SUMMARY AND DISCUSSION

In Fig. 19 we show a visual summary of the pasta phases found to coexist at increasing depth in the crust. Laterally, they are arranged with the minimum energy configuration on the left. To give a visualization of how the phases appear over longer length scales than a single cell, we have stacked four cells in each direction, but it is important to remember we only ever calculate one unit cell. We have not included every single density and configuration detailed in the previous section, but instead we selected those that best represent that region of density. Horizontal lines demarcate the four distinct regions we have identified, which we label P1–P4 in what follows. With increasing density, (P1) the region where pasta first appears as a local minimum, but isolated nuclei occupy the absolute minimum (P2) pasta phases have become consistently the absolute minimum but isolated nuclei still occupy local minima, (P3) all local minima correspond to pasta phases, while the protons are localized to the clusters in at least one dimension, (P4) all local minima correspond to pasta phases and protons are delocalized in all three dimensions.

One can trace the appearance and fate of one's favorite pasta shape with density. Isolated nuclei persist up to around 0.06 fm^{-3} but are demoted to local minimum at around 0.05 fm^{-3}. Isolated nuclei themselves may have exotic properties at high densities, with highly deformed nuclei aligning like liquid crystals. Spaghetti appears at low densities $\approx$0.04 fm^{-3} as a local minimum and is the most robust pasta shape, making appearances right up to densities of $\approx$0.088 fm^{-3}. It is most likely to be the absolute minimum at densities 0.05–0.06 fm^{-3}, appearing at local minima at most densities thereafter. Next, nuclear waffles appear as

a local minimum 0.05–0.06 fm^{-3} and persist over a wide density region up to close to 0.08 fm^{-3}. In our calculations, they appear as the global minimum at densities around 0.06 fm^{-3}. Nuclear waffles are a lasagna like phase—essentially lasagna modulated by density fluctuations along the plane of the shape. Lasagna appear at around 0.066 fm^{-3} and persist to the highest densities as local minima. Interestingly, lasagna never appear as the minimum energy configuration in our calculations; at the same density region they appear, so does the bicontinuous cubic-P phase, which appears to be energetically more stable and is the absolute minimum in the region 0.07–0.08 fm^{-3}, until being usurped by the phase that contains cylindrical holes. As discussed, the cylindrical hole phase we discover is actually a phases consisting of alternating cylindrical under—and over—densities, with neutrons and protons delocalized in the bulk. This is the absolute minimum up to the highest density we consider.

The exact phases that appear at each density are driven by the proton fraction and modulated by shell effects. To evolve through the pasta phases, one can either increase the density or the proton fraction, since protons promote clustering.

In Fig. 20 we plot the pressure [Fig. 20(a)] and chemical potential [Fig. 20(b)] at which we perform each of our calculations as a function of the densities of each local minimum as blue diamonds. We compare this with the pressure and neutron chemical potential as calculated with the compressible liquid drop model (CLDM) using the surface parameters that give closest agreement to 3DHF results (as described in Ref. [53]). First, we note that spurious shell effects caused by the discretization of the neutron energy spectrum and corresponding change in the density of states means we do not expect the pressure and neutron chemical potential to match exactly the CLDM results. Also, due to real shell effects, the equilibrium proton fraction differs from the CLDM result, and the pressure and neutron chemical potential depends on the proton fraction. Having said that, for most densities the pressures and neutron chemical potentials obtained in the 3DHF calculations well match the CLDM result, with the major differences being at intermediate densities.

The pressure can be translated approximately into a mass coordinate for the crust y, which is also approximately the column depth in the crust - the fraction of the mass of the
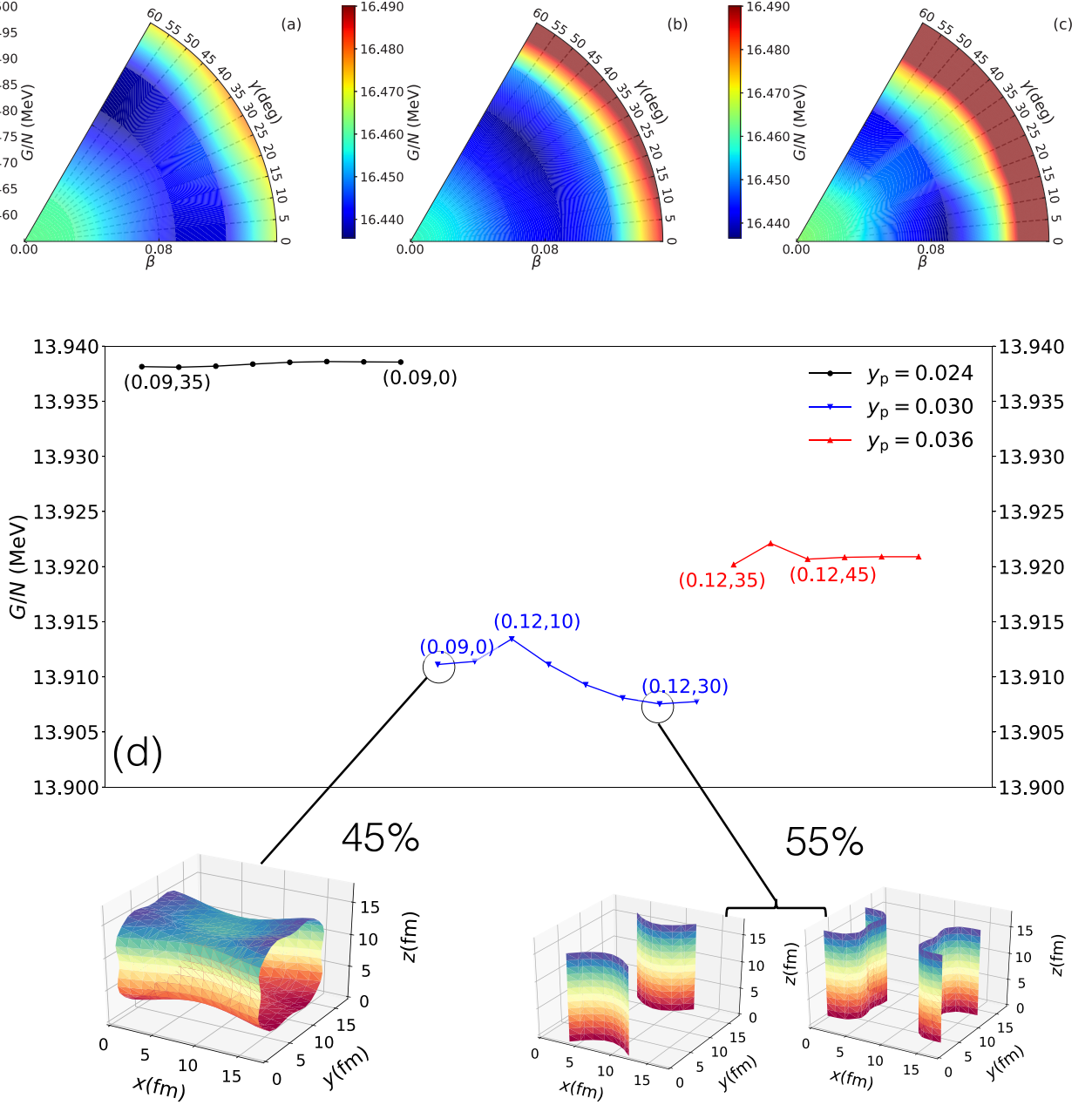
FIG. 17. Top row: Gibbs free-energy surfaces at a pressure of 0.45 MeV fm^{-3}, corresponding to a baryon density of ≈ 0.082 fm^{-3}, at proton fractions of 0.024 (a), 0.030 (b), and 0.036 (c), for cells containing $A_{\text{cell}} = 332$ nucleons. Below is the Gibbs free-energy variation along one dimensional paths passing through the energy minimum (d). Selected (β, γ) coordinates are shown along the one-dimensional plots. Visualizations of the minimum energy nuclear shapes are shown, obtained by plotting a surface of constant neutron density corresponding to the average neutron density in the cell. The first minimum is a combination of both a cylindrical high density and low density region (spaghetti and antispaghetti), whereas the second minimum is cylindrical. The relative abundances of the phases at a temperature equal to the fictive temperature is shown below the visualizations of the phases. In the simplified model we take a single barrier height to be the fictive temperature. These abundances will be frozen in as the temperature drops further unless quantum tunneling processes anneal the matter.

crust above a given layer at a given pressure. It is given by

$$y[P(\rho)] \equiv \frac{M_\star - M(P)}{M_\star} \approx \frac{P(\rho)}{P_{\text{cc}}}. \qquad (29)$$

Similarly, the neutron chemical potential at a particular density approximately determines the depth of the layer, and

we define the radial coordinate

$$r[\mu(\rho)] \equiv \frac{R_\star - R(\mu)}{R_\star} \approx \frac{\mu(\rho) + \mu_0}{\mu_{\text{cc}} + \mu_0}, \qquad (30)$$

where the subscript "cc" denotes the quantity at the crust-core transition, $M_\star$, $R_\star$ is the stellar radius and mass, and $M(P)$ and $R(\mu)$ the radius and mass out to the layer of the star characterized by the pressure P and chemical potential μ,
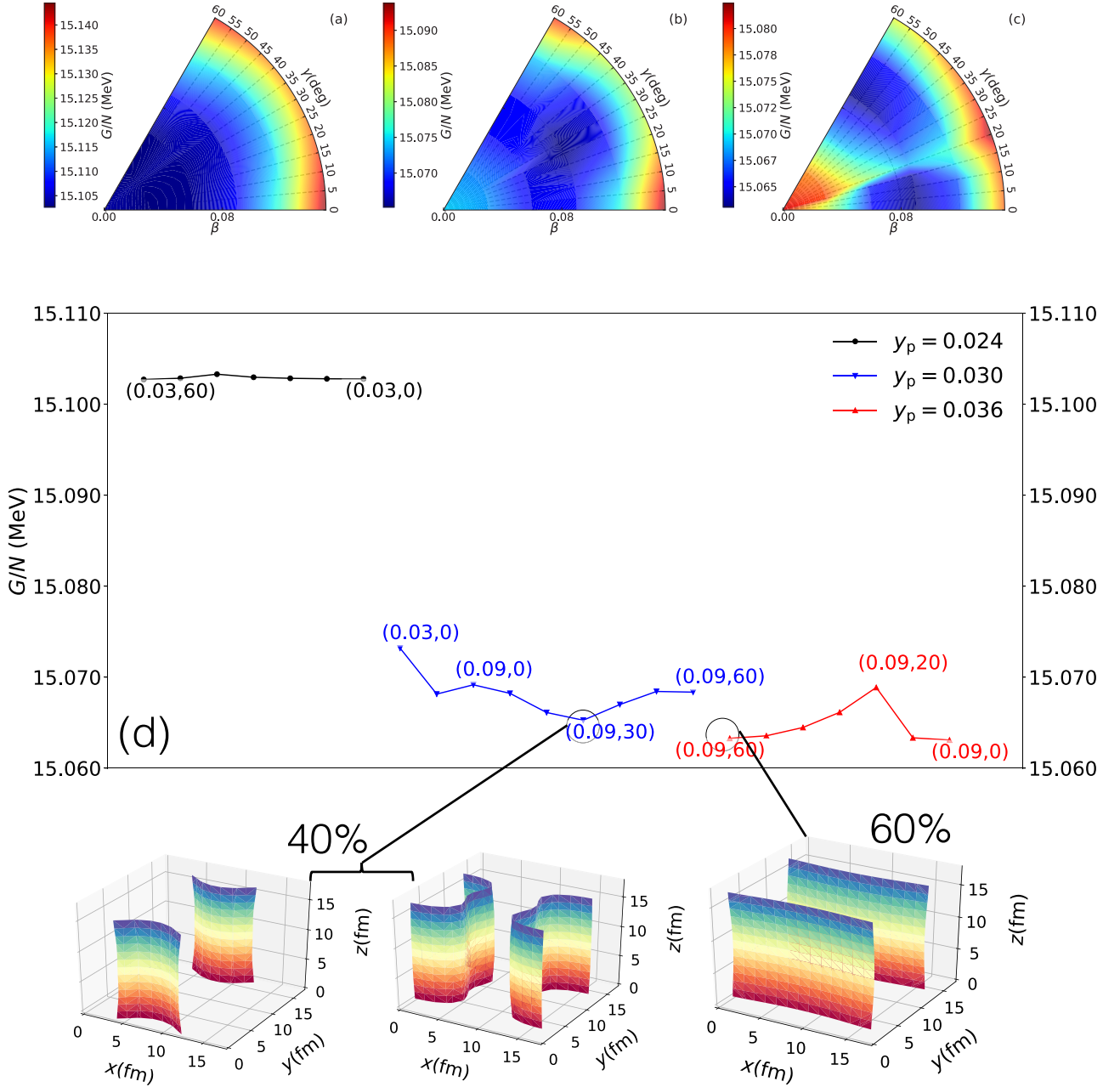
FIG. 18. Top row: Gibbs free-energy surfaces at a pressure of 0.53 MeV fm^{-3}, corresponding to a baryon density of ≈ 0.088 fm^{-3}, at proton fractions of 0.024 (a), 0.030 (b), and 0.036 (c), for cells containing $A_{\text{cell}} = 332$ nucleons. Below is the Gibbs free-energy variation along one dimensional paths passing through the energy minimum (d). Selected (β, γ) coordinates are shown along the one-dimensional plots. Visualizations of the minimum energy nuclear shapes are shown, obtained by plotting a surface of constant neutron density corresponding to the average neutron density in the cell. The first minimum is planar, and the second minimum is a combination of both a cylindrical high density and low density region (spaghetti and antispaghetti). The relative abundances of the phases at a temperature equal to the fictive temperature is shown below the visualizations of the phases.

respectively, and μ_0 the chemical potential at the surface of the star ≈ 9 MeV.

Our 3DHF calculations suggest that the crust-core transition density is ≈ 0.09 fm^{-3}. The CLDM results presented in Fig. 20 also give a transition density of 0.09 fm^{-3}. The CLDM crust-core transition pressure P_{cc} and chemical potential μ_{cc} are 0.54 MeV fm^{-3} and 13.6 MeV, respectively. The mass and radial coordinates y and m we display from

now on are obtained from the CLDM results. The mass and radius coordinates are a better measure of location in the crust, since density is not directly related to the depth in the crust (different EOSs will give different densities at a given depth or mass coordinate in the crust). In what follows, we plot various quantities versus y.

The plot of pressure versus density illustrates the size of the local average density fluctuations (the variation over
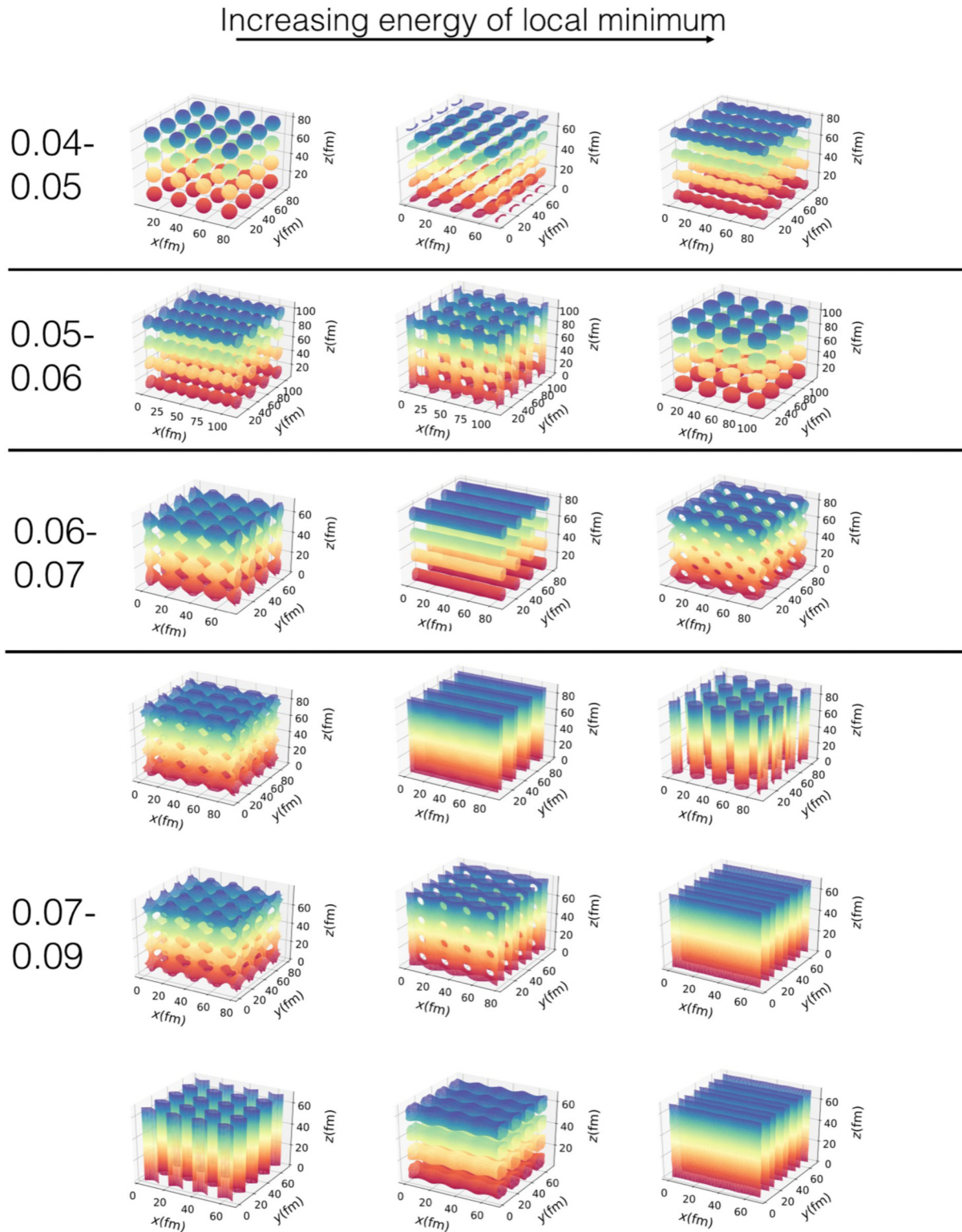
FIG. 19. Overview of all nuclear geometries that emerge from our calculations. To visualize the phases better we have plotted a region of four unit cells squared, but it is important to remember we only calculate one single unit cell. The colors are just for clarity of visualization and have no physical meaning. The left column gives the approximate baryon densities the configurations to the right cover. The minimum energy configurations are the leftmost pictures in each row, with the energy of the minimum increasing rightwards. We display only a representative selection of configurations. Horizontal lines divide the graphic into the four distinct regions of pasta: from low to high density, the region where pasta first appears as a local minimum at higher energy than the isolated nuclear phase; the region where pasta shapes become the absolute minimum, but isolated nuclei remain as higher energy local minima; the region where only pasta shapes exist; and the region where only pasta shapes exist, and protons have become delocalized in all dimensions.
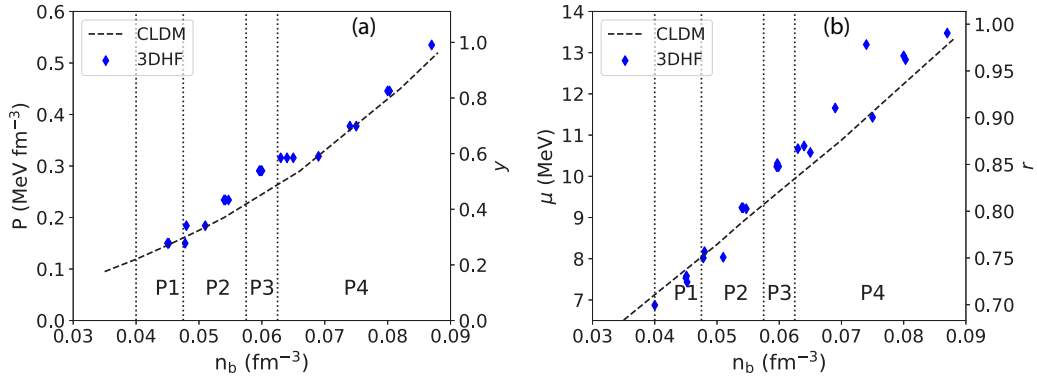
FIG. 20. (a) The pressure of matter in the crust as calculated by the compressible liquid drop model (dashed line), and the pressure of each of the configurations examined in our 3DHF calculations (blue diamonds). (b) The chemical potential from the CLDM and our 3DHF calculations. Vertical dotted lines divide the four regions of pasta P1-P4 as described in the text. The mass coordinate y calculated from the CLDM pressure is given in the right vertical scale in panel (a), and the radial coordinate r calculated from the CLDM chemical potential is given in the right vertical scale in panel (b).

the scale of the domain sizes). At $P = 0.33\,\mathrm{MeV\,fm^{-3}}$, for example, the density of the coexisting phases have a spread of $0.003\,\mathrm{fm^{-3}}$, about 5% of the average density. Typically the density fluctuations are between 2% and 5%.

In Fig. 20, the dotted vertical lines delineate the 4 distinct regions of pasta we identify: (P1) (pasta is a local minimum, spherical nuclei the ground state) accounts for about 10% of the crustal mass and 5% of the thickness, and spans a region between $\approx 20\%$ and 30% of the way into the crust by mass and $\approx 70\%$ and 75% by depth; (P2) (pasta is the ground state, spherical nuclei are local minima) accounts for about 15% of the crustal mass and 5% the crustal thickness, and spans a region between $\approx 30\%$ and 45% of the way into the crust by mass and $\approx 75\%$ and 80% by depth; (P3) (all local minima are pasta, protons are localized) accounts for about 5% of the crustal mass and thickness, and spans a region between $\approx 45\%$ and 50% of the way into the crust by mass and $\approx 80\%$ and 85% by depth; and (P4) (all local minima are pasta, protons are delocalized) accounts for about 50% of the crustal mass and 15% the crustal thickness, and spans a region between $\approx 55\%$ and 100% of the way into the crust by mass and $\approx 83\%$ and 100% by depth.

In Fig. 21, we plot the fictive temperature as a function of column depth y. The lower red points show the temperatures assuming the nucleons behave independently, and the upper blue diamonds assume that of order the proton number in the unit cell behave collectively when matter is rearranged from one pasta shape to another. There are a two main contributors to the energy barriers: the lattice energy caused by the Coulomb repulsion of the protons in adjacent pasta structures, and the shell energy. Rearranging the pasta configuration requires a rearrangement of nucleons in the vicinity of the Fermi surface of order the proton number.

The fictive temperature is calculated based on the average barrier heights between local minima in our calculations; the bars on each points indicate the range of barrier heights at each depth.

The lower limit to the barrier heights given by the red points start around 10^9 K and drop to $\sim 10^8$ K throughout most of the pasta region, dropping down below 10^8 K at in the final 20% of the crust by mass. The estimates assuming a realistic number of nucleons behaving collectively are an order of magnitude higher.

When the crust temperature drops below this temperature, the coexisting pasta domains are frozen in with respect to thermal fluctuations, at their equilibrium abundances and characteristic lengths at the fictive temperature. Quantum tunneling could then anneal the crust on a timescale that is yet to be determined, the end result being a single phase of pasta at each depth. Future heating could then repopulate the local
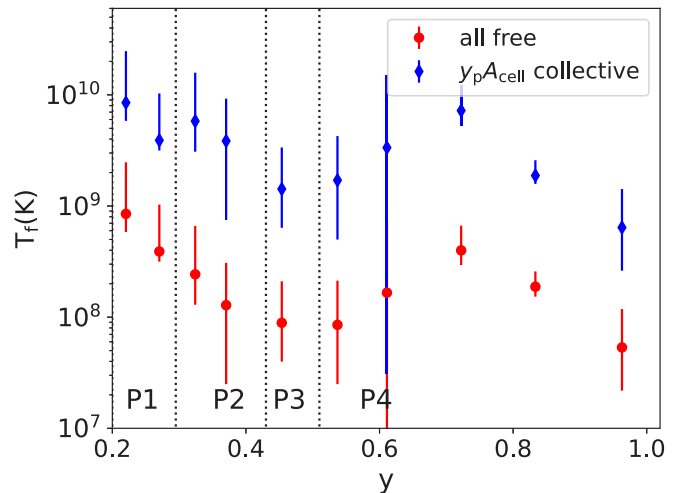

FIG. 21. The fictive temperature T_f as a function of mass coordinate in the crust y (the fraction of the mass of the crust above a given point) assuming that the relevant degrees of freedom are individual nucleons (red points), or a collection of nucleons of order the proton number $y_p A_{cell}$ (blue diamonds). The bars span the range of of barrier heights from our calculations. Vertical dotted lines divide the four regions of pasta P1–P4 as described in the text.
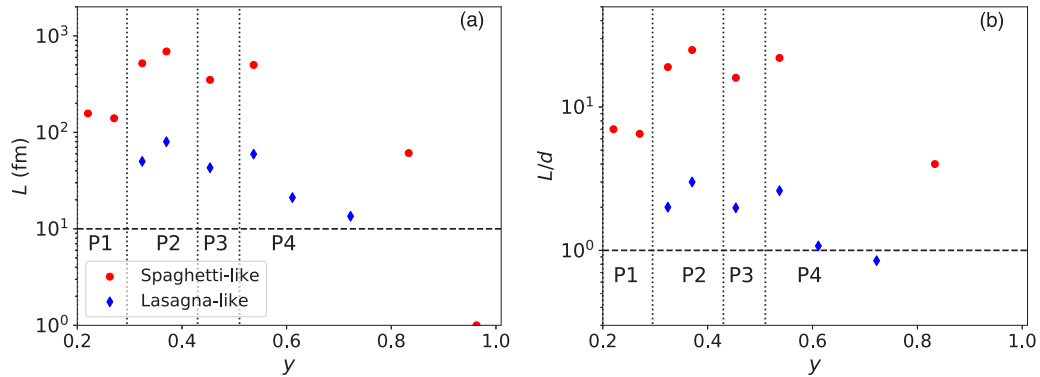
FIG. 22. The long-range order of the pasta phases ΔL calculated at the fictive temperature, assuming individual nucleons are the relevant degrees of freedom, as a function of mass parameter. We give the length scale in absolute terms (a) and in units of cell size (b). The horizontal dashed lines indicate the point where the order drops below 10 fm—approximately the characteristic width of nuclear clusters (a)—and below one cell size (b). Spaghettilike configurations are shown as red pints, and lasagnalike configurations are shown by blue diamonds. At high y the Lasagna order becomes much less than the cell size, too low to appear on the plots; at that point the formalism used to calculate the disorder breaks down. Below the dashed lines, matter is completely disordered. These are *upper* limits on the long-range order: if we assume that clusters of nucleons are the relevant degrees of freedom, then the fictive temperature increases (see Fig. 21) and the long-range order drops. Vertical dotted lines divide the four regions of pasta P1–P4 as described in the text.

minima. It is interesting to note that direct Urca and neutrino-antineutrino pair emission processes in pasta phases become competitive with modified Urca processes in bulk matter at temperatures below 10^9 K [76], and so may quickly drive the temperature of the pasta phases below the fictive temperature and into the frozen/annealing phase.

The length scales of the domains at the fictive temperature are plotted in Fig. 22. Here we take the low end of the bound on the fictive temperature from the red points in Fig. 21: this gives an *upper* limit to the domain sizes at the time the domains freeze. We plot the size of the domains as a function of mass coordinate in absolute terms [Fig. 22(a)] and in units of lattice spacings d [Fig. 22(b)]. Dashed horizontal lines indicate where the order falls below 10 fm [Fig. 22(a)]—a typical width of pasta structures—and below one lattice spacing [Fig. 22(b)]. These lines indicate the scale below which the phases become completely disordered—essentially liquid. The temperature at which the order corresponds to these lines is the melting temperature of the glassy pasta. Spaghettilike configurations are shown as red points and lasagnalike configurations as blue diamonds. Spaghetti phases generally have long-range order of at most between 100 and 1000 fm (10–50 lattice spacings), with the longest range order occurring in regions P2 and P3. Lasagnalike phases are an order of magnitude less ordered, peaking at 80 fm ($\approx$3 lattice spacings) and dipping down to below the melting point in the deepest layers.

Given these are *upper* limits, we can conclude that the pasta phases are highly disordered at the fictive temperature, which supports the hypothesis that they have very high thermal and electrical resistivity. Additionally, given the domains are only ordered over a short range, electron scattering from domain boundaries could contribute significantly to the thermal and electrical resistivity of the deep layers of the crust.

As the temperature drops below the fictive temperature, the domains are frozen and cannot immediately grow in size, being bounded by adjacent domains. If annealing occurs, then the domains containing lower energy phases will

gradually grow as they convert surrounding higher energy phases.

If the crust gets heated above the fictive temperature, then thermal fluctuations can once again repopulate the local minima. The base of the crust is expected to be heated up to temperatures of order 10^8 K during accretion, enough to enter the regime where different phases could be repopulated and coexist. If a stage is reached where an entire layer has been completely annealed, then increases in temperature even below the fictive temperature will decrease the long-range order. In either case, the thermal conductivity could be temperature dependent, something that might be explored in crust cooling simulations.

One of the crucial quantities in determining the stability of phases is the lattice Coulomb energy per particle W_{CL}/A, which we plot in Fig. 23 as a function of column density y for all local minima. The lattice energy rises to a peak at a mass fraction of around 0.4 (a density of around $0.06\,\mathrm{fm}^{-3}$), corresponding to the region where isolated nuclei have vanished from the energy landscape, and the energy surfaces have their most structure. From then on, the lattice energy decreases roughly exponentially up to the crust-core transition. It should vanish completely at the crust-core transition, but density fluctuations due to the spurious shell effects mean that it remains finite in our calculations.

V. CONCLUSIONS

We have conducted a large set of quantum calculations of nuclear pasta using the three-dimensional Hartree-Fock method with the NRAPR Skyrme interaction and BCS pairing. A quadrupole constraining potential allowed us to control the shape of the nuclear deformation, and therefore systematically probe the energy landscape of nuclear pasta. Although the constraint determines the shape we get, by ranging over the whole parameter space of the quadrupole deformation, we
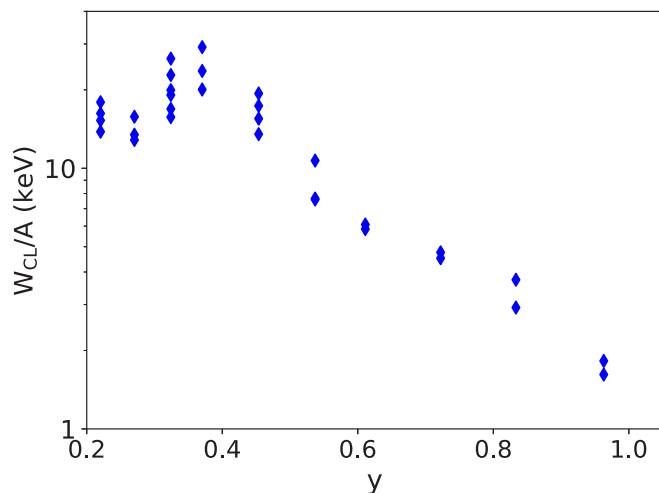
FIG. 23. The lattice energy per nucleon in the unit cell for minimum energy configurations as a function of mass coordinate y. The lattice energy drives the stability of the phases; it peaks at around $y = 0.4$ (a baryon density of $\approx 0.06 \, \text{fm}^{-3}$), where isolated nuclei disappear from the minima in the energy landscape, and then decreases roughly exponentially with density thereafter.

were able to reproduce and compare all pasta shapes in an unbiased way.

We selected 11 different density regimes to perform calculations at, ranging from $0.035 \, \text{fm}^{-3}$ to $0.088 \, \text{fm}^{-3}$. At each density we selected a single cell size, chosen based on the range of cell sizes predicted by calculations using the compressible liquid drop model (CLDM). In each density regime we performed calculations at five different, closely spaced densities and used the results to interpolate the energy at a given reference pressure, chosen to be the pressure for a zero-deformation configuration at the central density in the range. We thus calculated the Gibbs free energy, and were able to compare configurations in equilibrium at constant pressure (and therefore at the same depth in the crust). In each density regime we also performed calculations over a range of proton fractions to locate the β-equilibrium proton fraction. In total, the results we show are obtained from approximately 30,000 calculations and 300,000 CPU hours.

We show that the energy landscape consists of multiple local minima corresponding to different nuclear geometries with very similar energies, separated by barriers of 1-100 keV which generally decrease with depth. These findings are consistent with earlier, more limited explorations of the energy landscape of nuclear pasta [16]. The various minima at a given depth can be at different proton fractions and densities. Therefore, at a given depth in the star, multiple nuclear pasta shapes may coexist, and there may be local variations of the average electron fraction and baryon density of order 10% and 1–5%, respectively.

The following nuclear geometries were found: spherical and deformed nuclei appear up to $n_b = 0.06 \, \text{fm}^{-3}$ as either the minimum energy configuration (up to $n_b \approx 0.05 \, \text{fm}^{-3}$) or a local minimum. Spaghetti appears over

the range 0.04–$0.088 \, \text{fm}^{-3}$, the waffle phase (perforated planes) appear over the range 0.05–$0.08 \, \text{fm}^{-3}$, lasagna over 0.065–$0.088 \, \text{fm}^{-3}$, the bicontinuous cubic-P (BCP) phase over the range 0.066–$0.08 \, \text{fm}^{-3}$ and cylindrical holes appear at 0.08–$0.088 \, \text{fm}^{-3}$. The BCP phase consists of both continuous neutron matter and nuclear matter interlaced; the protons are therefore delocalized in all directions. The cylindrical holes coexist with spaghetti phases, with protons delocalized in the bulk. At each depth in the crust we identify the phases that coexist and estimate their relative abundances. Spaghetti appears over the widest range of densities.

Four distinct regions can be identified, which we denote P1–P4: (P1) roughly spherical nuclei are the minimum energy configuration, but pasta appears as local minima; (P2) pasta phases become the minimum energy configuration, but spherical nuclei still occupy some local minima; (P3) all local minima correspond to pasta configurations, and protons are localized in at least one dimension; and (P4) all local minima correspond to pasta configurations, and the appearance of the BCP phase indicates protons are delocalized in all dimensions. We find the BCP phase is particularly stable and the delocalized proton region accounts for at least half of the pasta layers by mass and 15% by depth. The regions P2–P4—where pasta is the ground state—occupy about 70% of the whole crust by mass and 25% by depth. In total, P1–P4 accounts for almost 80% of the mass of the crust and 30% of its thickness. When protons become delocalized they are free to carry currents and maybe form a type-II superconductor [77].

The nature of the energy landscape suggests the pasta phases are glassy: they undergo a transition to an amorphous solid at a certain temperature below their melting temperature. We take the barrier heights between local minima to set the temperature scale - the so-called fictive temperature, to borrow a term from condensed matter physics, above which matter is an amorphous solid. As matter cools below the fictive temperature, we posit that it becomes frozen into domains with a length scale set by stability against thermal fluctuations at the fictive temperature. These length scales are of order 10 times the cell size at lower depths, falling to below the cell size at higher depths, depending on whether the nuclear geometry is spaghettilike or lasagnalike. If the length scale is below the cell size, then the matter remains a liquid (no long-range order at all) until the temperature cools significantly below the fictive temperature.

Once matter is frozen into domains, it is possible annealing will begin to homogenize the matter at a given depth, with domains corresponding to the marginally energetically preferred configuration expanding their volume, converting the other phases. The conversion process could be similar to pycnonuclear fusion [78,79], whose timescale uncertainty is many orders of magnitude (see, for example, Table 2 in Ref. [80]). Additionally, domains many times the size of a single unit cell will need to be converted. An analysis of the uncertainty this leads to on the annealing timescale would be an important future study to undertake. Annealing would release heat in the deep layers of the crust of order 1–50 keV/nucleon—the

typical energy differences between local minima and the ground state.

Although we perform a very large number of calculations, we still do not sample widely the unit cell size at any given depth, and although it is reasonable to expect that our results do not qualitatively depend on cell size, it is likely that some phases we do not see (notably bubble) are missed due to this restriction. Phases that never appear as the minimum energy configuration in our calculations—like spaghetti—likely would in a larger set of calculations. In a recent set of calculations using the same method at fixed proton fractions, and generally larger cell sizes, a similar set of pasta geometries were found [8]. Our results should be taken as an illuminating snapshot of the pasta landscape. As noted in the methods section, we have tested that the same pasta phases are obtained when we double the length of the cell in a single direction, and calculations in cells of eight times the volume and more are ongoing, in part to test the cell size dependence of the pasta shapes further.

The phases of pasta present depend on the proton fraction, which in turn depends on the symmetry energy at pasta densities. An examination of the dependence of our results on the EOS—particularly, the extent of the four distinct regions of pasta—will be presented in an upcoming work.

As we explore the nuclear pasta phases in more detail, their structure at both micro- and mesoscales becomes richer and more complex, presenting a serious challenge to modeling the material and transport properties near the crust-core boundary. However, the fact they likely occupy a large mass fraction and thickness of the crust, and that they mediate the transition from solid crust to liquid core, means they remain an essential ingredient in the modeling of many macroscopic, observable neutron star phenomena.

[1] M. E. Caplan and C. J. Horowitz, Rev. Mod. Phys. **89**, 041002 (2017).

[2] R. A. L. Jones, Eur. J. Phys. **23**, 652 (2002).

[3] D. Q. Lamb, J. M. Lattimer, C. J. Pethick, and D. G. Ravenhall, Phys. Rev. Lett. **41**, 1623 (1978).

[4] D. G. Ravenhall, C. J. Pethick, and J. R. Wilson, Phys. Rev. Lett. **50**, 2066 (1983).

[5] M. Hashimoto, H. Seki, and M. Yamada, Prog. Theor. Phys. **71**, 320 (1984).

[6] K. Oyamatsu, M. Hashimoto, and M. Yamada, Prog. Theor. Phys. **72**, 373 (1984).

[7] A question is whether to continue the proliferation of pasta nomenclature. We come down on the side of yes!

[8] F. J. Fattoyev, C. J. Horowitz, and B. Schuetrumpf, Phys. Rev. C **95**, 055804 (2017).

[9] F. Ji, J. Hu, S. Bao, and H. Shen, Phys. Rev. C **102**, 015806 (2020).

[10] A. S. Schneider, D. K. Berry, C. M. Briggs, M. E. Caplan, and C. J. Horowitz, Phys. Rev. C **90**, 055805 (2014).

[11] D. K. Berry, M. E. Caplan, C. J. Horowitz, G. Huber, and A. S. Schneider, Phys. Rev. C **94**, 055801 (2016).

[12] K. Nakazato, K. Oyamatsu, and S. Yamada, Phys. Rev. Lett. **103**, 132501 (2009).

[13] K. Nakazato, K. Iida, and K. Oyamatsu, Phys. Rev. C **83**, 065811 (2011).

[14] B. Schuetrumpf and W. Nazarewicz, Phys. Rev. C **92**, 045806 (2015).

[15] C. J. Pethick and A. Y. Potekhin, Phys. Lett. B **427**, 7 (1998).

[16] P. Magierski and P.-H. Heenen, Phys. Rev. C **65**, 045804 (2002).

[17] P. Gögelein and H. Müther, Phys. Rev. C **76**, 024312 (2007).

[18] P. Gögelein, E. N. E. van Dalen, C. Fuchs, and H. Müther, Phys. Rev. C **77**, 025802 (2008).

[19] P. Grygorov, P. Gögelein, and H. Müther, J. Phys. G: Nucl. Part. Phys. **37**, 075203 (2010).

[20] W. G. Newton and J. R. Stone, Phys. Rev. C **79**, 055801 (2009).

[21] H. Pais and J. R. Stone, Phys. Rev. Lett. **109**, 151101 (2012).

[22] B. Schuetrumpf, M. A. Klatt, K. Iida, J. A. Maruhn, K. Mecke, and P.-G. Reinhard, Phys. Rev. C **87**, 055805 (2013).

[23] B. Schuetrumpf, K. Iida, J. A. Maruhn, and P.-G. Reinhard, Phys. Rev. C **90**, 055802 (2014).

[24] B. Schuetrumpf, M. A. Klatt, K. Iida, G. E. Schröder-Turk, J. A. Maruhn, K. Mecke, and P.-G. Reinhard, Phys. Rev. C **91**, 025801 (2015).

[25] I. Sagert, G. I. Fann, F. J. Fattoyev, S. Postnikov, and C. J. Horowitz, Phys. Rev. C **93**, 055801 (2016).

[26] B. Schuetrumpf, W. Nazarewicz, and P.-G. Reinhard, Phys. Rev. C **93**, 054304 (2016).

[27] B. Schuetrumpf, G. Martínez-Pinedo, Md. Afibuzzaman, and H. M. Aktulga, Phys. Rev. C **100**, 045806 (2019).

[28] B. Schuetrumpf, G. Martínez-Pinedo, and P. G. Reinhard, Phys. Rev. C **101**, 055804 (2020).

[29] T. Maruyama, K. Niita, K. Oyamatsu, T. Maruyama, S. Chiba, and A. Iwamoto, Phys. Rev. C **57**, 655 (1998).

[30] H. Sonoda, G. Watanabe, K. Sato, K. Yasuoka, and T. Ebisuzaki, Phys. Rev. C **77**, 035806 (2008).

[31] C. J. Horowitz, M. A. Pérez-García, and J. Piekarewicz, Phys. Rev. C **69**, 045804 (2004).

[32] C. J. Horowitz, M. A. Pérez-García, D. K. Berry, and J. Piekarewicz, Phys. Rev. C **72**, 035801 (2005).

[33] C. J. Horowitz and D. K. Berry, Phys. Rev. C **78**, 035806 (2008).

[34] A. S. Schneider, C. J. Horowitz, J. Hughto, and D. K. Berry, Phys. Rev. C **88**, 065807 (2013).

[35] M. E. Caplan, A. S. Schneider, C. J. Horowitz, and D. K. Berry, Phys. Rev. C **91**, 065802 (2015).

[36] A. S. Schneider, D. K. Berry, M. E. Caplan, C. J. Horowitz, and Z. Lin, Phys. Rev. C **93**, 065806 (2016).

[37] M. E. Caplan, A. S. Schneider, and C. J. Horowitz, Phys. Rev. Lett. **121**, 132701 (2018).

[38] A. S. Schneider, M. E. Caplan, D. K. Berry, and C. J. Horowitz, Phys. Rev. C **98**, 055801 (2018).

[39] Z. Lin, M. E. Caplan, C. J. Horowitz, and C. Lunardini, Phys. Rev. C **102**, 045801 (2020).

[40] R. Nandi and S. Schramm, Phys. Rev. C **94**, 025806 (2016).

[41] R. Nandi and S. Schramm, Astrophys. J. **852**, 135 (2018).

[42] R. Nandi and S. Schramm, J. Astrophys. Astron. **39**, 40 (2018).

[43] C. O. Dorso, P. A. Giménez Molinelli, and J. A. López, Phys. Rev. C **86**, 055805 (2012).

[44] P. A. Giménez Molinelli, J. I. Nichols, J. A. López, and C. O. Dorso, Nucl. Phys. A **923**, 31 (2014).

[45] C. O. Dorso, G. A. Frank, and J. A. López, Nucl. Phys. A **978**, 35 (2018).

[46] J. A. López, C. O. Dorso, and G. Frank, Front. Phys. **16**, 24301 (2021).

[47] M. E. Caplan, C. R. Forsman, and A. S. Schneider, Phys. Rev. C **103**, 055810 (2021).

[48] D. G. Yakovlev, M. E. Gusakov, and P. Haensel, Mon. Not. R. Astron. Soc. **481**, 4924 (2018).

[49] D. N. Kobyakov and C. J. Pethick, J. Exper. Theor. Phys. **127**, 851 (2018).

[50] C. J. Pethick, Z.-W. Zhang, and D. N. Kobyakov, Phys. Rev. C **101**, 055802 (2020).

[51] G. Watanabe, K. Iida, and K. Sato, Nucl. Phys. A **676**, 455 (2000).

[52] C. P. Lorenz, D. G. Ravenhall, and C. J. Pethick, Phys. Rev. Lett. **70**, 379 (1993).

[53] L. Balliet, W. Newton, S. Cantu, and S. Budimir, Astrophys. J. **918**, 79 (2021).

[54] C. J. Horowitz, D. K. Berry, C. M. Briggs, M. E. Caplan, A. Cumming, and A. S. Schneider, Phys. Rev. Lett. **114**, 031102 (2015).

[55] J. A. Pons, D. Viganò, and N. Rea, Nat. Phys. **9**, 431 (2013).

[56] M. Bender, P. Heenen, and P. Reinhard, Rev. Mod. Phys. **75**, 121 (2003).

[57] A. W. Steiner, M. Prakash, J. M. Lattimer, and P. J. Ellis, Phys. Rep. **411**, 325 (2005).

[58] R. Y. Cusson, P. G. Reinhard, M. R. Strayer, J. A. Maruhn, and W. Greiner, Z. Phys. A **320**, 475 (1985).

[59] M. Frigo and S. G. Johnson, *FFTW: Fastest Fourier Transform in the West* (MIT Press, Cambridge, MA, 2012).

[60] D. Baye and P. H. Heenen, J. Phys. A: Math. Gen. **19**, 2041 (1986).

[61] J. W. Negele and D. Vautherin, Nucl. Phys. A **207**, 298 (1973).

[62] M. Bender, K. Rutz, P. G. Reinhard, and J. A. Maruhn, Eur. Phys. J. A **8**, 59 (2000).

[63] P. Bonche, H. Flocard, P. H. Heenen, S. J. Krieger, and M. S. Weiss, Nucl. Phys. A **443**, 39 (1985).

[64] K. T. R. Davies, H. Flocard, S. Krieger, and M. S. Weiss, Nucl. Phys. A **342**, 111 (1980).

[65] P. G. Reinhard and R. Y. Cusson, Nucl. Phys. A **378**, 418 (1982).

[66] W. Greiner, J. A. Maruhn, and D. A. Bromley, *Nuclear Models* (Springer, London, 1997).

[67] W. G. Newton, Ph.D. Thesis, University of Oxford, 2008.

[68] K. Hebeler, J. M. Lattimer, C. J. Pethick, and A. Schwenk, Astrophys. J. **773**, 11 (2013).

[69] S. Gandolfi, J. Carlson, S. Reddy, A. W. Steiner, and R. B. Wiringa, Eur. Phys. J. A **50**, 10 (2014).

[70] S. Gandolfi, A. Gezerlis, and J. Carlson, Annu. Rev. Nucl. Part. Sci. **65**, 303 (2015).

[71] I. Tews, S. Gandolfi, A. Gezerlis, and A. Schwenk, Phys. Rev. C **93**, 024305 (2016).

[72] C. Drischler, K. Hebeler, and A. Schwenk, Phys. Rev. C **93**, 054314 (2016).

[73] W. G. Newton, M. Gearheart, and B.-A. Li, Astrophys. J. Supp. Ser. **204**, 9 (2013).

[74] J. C. Mauro, R. J. Loucks, and P. K. Gupta, J. Am. Ceram. Soc. **92**, 75 (2009).

[75] N. Chamel, Nucl. Phys. A **747**, 109 (2005).

[76] W. G. Newton, K. Murphy, and B.-A. Li, Astrophys. J. Lett. **779**, L4 (2013).

[77] Z.-W. Zhang and C. J. Pethick Phys. Rev. C **103**, 055807 (2021).

[78] D. G. Yakovlev, L. R. Gasques, M. Beard, M. Wiescher, and A. V. Afanasjev, Phys. Rev. C **74**, 035803 (2006).

[79] D. G. Yakovlev, M. Beard, L. R. Gasques, and M. Wiescher, Phys. Rev. C **82**, 044609 (2010).

[80] D. G. Yakovlev, L. Gasques, and M. Wiescher, Mon. Not. R. Astron. Soc. **371**, 1322 (2006).